INL/RPT-23-75257

Printed Strain Gauges for High Temperature Applications (>300°C)

October 2023

Advanced Sensors and Instrumentation Program

Timothy L. Phero
Energy and Environmental Science and Technology, Idaho National Laboratory

Amey R. Khanolkar
Energy and Environmental Science and Technology, Idaho National Laboratory

Michael D. McMurtrey
Nuclear Science and Technology, Idaho National Laboratory

Idaho National Laboratory

INL is a U.S. Department of Energy National Laboratory
operated by Battelle Energy Alliance, LLC

INL/RPT-23-75257
Revision 0

Printed Strain Gauges for High Temperature Applications (>300°C)

Advanced Sensors and Instrumentation Program

Timothy L. Phero

Energy and Environmental Science and Technology, Idaho National Laboratory

Amey R. Khanolkar

Energy and Environmental Science and Technology, Idaho National Laboratory

Michael D. McMurtrey

Nuclear Science and Technology, Idaho National Laboratory

October 2023

Idaho National Laboratory
Idaho Falls, Idaho 83415

http://www.inl.gov

Prepared for the
U.S. Department of Energy
Office of Nuclear Energy
Under DOE Idaho Operations Office
Contract DE-AC07-05ID14517

Page intentionally left blank

ABSTRACT

The real-time understanding of strain and deformation of materials provides prognostic health monitoring of components of current operational reactors and valuable data that shortens the timeline for the development of new nuclear-relevant materials in test reactor experiments. This report discusses the current status of the development and testing of additively manufactured strain gauges for operation at elevated temperatures. This has potential to improve the sensor design and manufacturing techniques to meet the requirements of active in-pile sensing in current and advanced nuclear reactors (i.e., in terms of environment conditions, sample geometry, and materials compatibility). The developmental additively manufactured strain gauges are exposed to separate effects testing (i.e., mechanical strain, high temperature) to determine environmental factors that affect the strain gauge. In addition, sensor qualification methodologies are further developed for determining the reliability and robustness at the interface of the AM strain gauge materials.

Page intentionally left blank

ACKNOWLEDGEMENTS

The authors gratefully acknowledge the support provided by Kaelee Novich, Brian J. Jaques, and David Estrada of Boise State University. The authors would also like to thank Michael Heighes from the Nuclear Science and Technology Directorate at Idaho National Laboratory (INL) for support with mechanical testing. The authors would finally like to express their gratitude to James Smith, Bradley Benefiel and Shaun Evans from the Nuclear Science and Technology Directorate at INL for their help running the laser spallation testing. This work was supported through the Department of Energy (DOE) Advanced Sensors and Instrumentation program under DOE Idaho Operations Office Contract DE-AC07-05ID14517. The views and opinions of authors expressed herein do not necessarily state or reflect those of the U.S. Government or any agency thereof.

Page intentionally left blank

CONTENTS

FIGURES

TABLES

ACRONYMS

AM	Additive manufacturing
AJP	Aerosol jet printing
BST	Barium strontium titanate
CSG	Capacitive strain gauge
CTE	Coefficient of thermal expansion
EDS	Energy dispersive x-ray spectroscopy
FEA	Finite element analysis
IDE	Interdigitated electrode
INL	Idaho National Laboratory
LSS	Laser Shock System
MEMS	Microelectromechanical
PVC	Polyvinyl chloride
RSG	Resistive strain gauge
RT	Room temperature
SEM	Scanning electron microscopy
STR	Strain transfer ratio

Page intentionally left blank

Printed Strain Gauges for High Temperature Applications (>300°C)

1. INTRODUCTION

Advancements in additive manufacturing (AM) techniques have the potential to revolutionize in-pile and out-of-pile measurements by enabling the direct fabrication of sensors on fuels, cladding, and structural materials. AM provides opportunities to develop sensors with a wide range of materials and mitigates the complex, expensive fabrication processes found in conventional thin-film and photolithography procedures [1, 2]. Over the last couple of years, AM using aerosol jet printing (AJP) has demonstrated the capability to fabricate in-pile passive monitors used for determining peak temperatures [3], which shows the ability to formulate printed ink materials that have specific design needs and requirements (e.g., melting temperatures). In addition, AM sensor devices have shown that they can overcome the challenges associated with high temperature environments (above 300°C [4]) and components with non-planar, cylindrical geometries [5] that are commonly found in nuclear reactors. In AJP, as shown in Figure 1, a colloidal nanoparticle suspension is aerosolized using an ultrasonic transducer via high-frequency pressure waves that are transmitted through the ink vial. The aerosolized ink is carried to the nozzle-head assembly by an inert carrier gas through an ink tube. The aerosolized ink is then focused into a fine beam with an inert sheath gas, which is deposited onto a substrate. The focused beam allows for deposition of features down to 10 µm resolution [6], which enables the miniaturization of current sensing technologies. AJP can also fabricate sensors with a wide range of customized nuclear-relevant ink material systems, or any inks with viscosities ranging between 1 – 2500 cP [7] on a variety of planar and non-planar substrate geometries [5, 8]. The design flexibility and rapid fabrication capabilities of AJP make it an ideal tool for prototyping miniaturized, non-intrusive strain sensors with specialized design requirements for nuclear reactor applications.

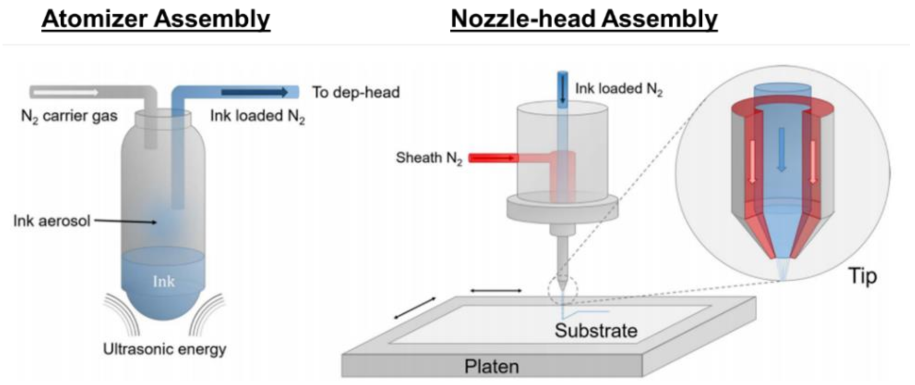

Figure 1. Schematic of the aerosol jet printing system with ultrasonic atomization [9]

Recently, AJP was used to fabricate interdigitated electrode (IDE) capacitance-based strain gauges (CSG) and were shown to have enhanced performance in high strain conditions as compared to commercially-available high-elongation resistive strain gauges [10]. The IDE design (Figure 2) enables for a low-profile CSG with multiple in-plane electrodes that are parallel to the substrate, which have been observed to have high strain sensitivity [11, 12]. In addition, the capacitive sensing mechanism of CSGs have shown to be better suited for long-term static measurements in harsh environments due to its low hysteresis and low environmental sensitivity to high-temperature degradation effects (e.g., oxidation) that affect the electrical performance of RSGs [4, 10, 13, 14]. The low-profile nature, high temperature compatibility, and suitability for wireless signal transmission [12, 15] make the IDE CSG a promising design for strain gauges in harsh environments.

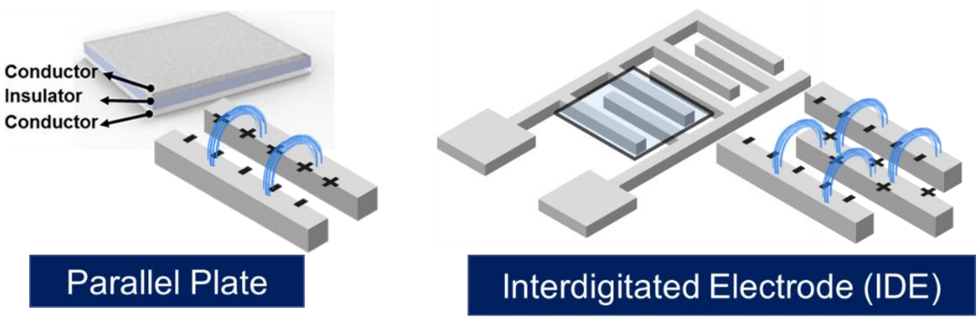

Figure 2. Two different capacitive sensor design types including parallel plate and interdigitated electrode.

In a reactor system, strain sensing devices must maintain electrical stability and strain sensitivity, while also maintaining a small form factor to avoid disrupting the functionality of a reactor's native surroundings. Current strain gauges are restricted by their size, non-trivial integration methods (i.e., welding), and modes (i.e., wired and/or wireless) to transmit the measured signal. As shown in Table 1, current developmental work on IDE CSGs is limited to testing on flexible polymer substrates at room temperature and at high strain levels (above 3,000 $\mu\varepsilon$) [11, 12, 16-20]. Work that tested the IDE CSG at temperatures above room temperature showed results for a limited sample size, and employed conventional fabrication methods (i.e., lithography and sputtering) that are expensive and limited to flat, rigid substrates with small sample geometries [21]. In this report, the current development of IDE CSGs that are fabricated on structural materials (i.e., aluminum 6061-T6 and stainless steel 316) and tested up to moderate temperature (i.e., 300°C) and high temperature (i.e., 500°C) environments are discussed.

This report will be split into three sections: **1)** testing of AM printed strain gauges up to 300°C (*Section 3*), **2)** testing of AM printed strain gauges up to 500°C (*Section 4*), and **3)** development of quality control metrics for testing the robustness and reliability of AM printed strain gauges (*Section 5*). Sections 3 and 4, in this work, increase the efficacy of AM IDE CSGs by developing and demonstrating methods to reliably fabricate high temperature strain gauges with aerosol jet printing. To measure the reliability and robustness of the sensor materials interface, Section 5 will discuss the development and implementation of quality control metrics through adhesion testing. The multi-materials system of AM sensors presents challenging chemical and physical interactions that warrant thorough characterization prior to deployment in critical reactor experiments. Detailed investigations of the performance of IDE CSGs (that includes their temperature-dependent strain sensitivity and hysteresis) in a controlled out-of-pile (laboratory) environment above room temperature is a vital step towards their development and qualification for in-pile strain sensing. A strong adhesive bond between the strain gage and the component being tested ensures efficient strain transfer from the component to the strain gage [22]. Strong adhesion between the various printed layers of the strain gage also reduces the likelihood of premature failure of the strain gage in service [22]. In addition to characterizing material interactions and the performance of AM printed IDE CSGs, ensuring robust interlayer adhesion between the various components of the printed CSG as well as between the strain gage and the substrate itself, is therefore a prerequisite to reliable strain measurement. To this end, a comparison of the non-contact laser-based and contact adhesion test methods, including implementation, differences, and limitations, has not been previously studied as far as the authors are aware. Adhesion testing, amongst other possible quality control metrics, provides vital feedback on the durability of the printed layers that can aid the successful deployment of AM sensor devices including IDE CSGs.

Table 1. Comparison of previously reported work on interdigitated electrode capacitance-based strain gauges. *T and C represent tensile and compressive mechanical loading, respectively. [3]

	Materials	Fabrication Technique	Working Environment	Strain level ($\mu\varepsilon$)*	Gauge Factor	References
1	Silver nanowires on polydimethylsiloxane (PDMS)	Capillary force lithography	RT	0 to 300,000 (T)	2.0	[11]
2	Carbon nanotubes on polydimethylsiloxane (PDMS)	Lithography	RT	0 to 3,500 (T/C)	3.4 – 4.9	[16]
3	Gold electrodes and nanoparticles on polyimide substrate	Lithography and drop casting	RT	0 to 20,000 (T)	0.1 - 3.8	[12]
4	Copper in flexible epoxy resin attached to tire surface and glass fiber-reinforced polymer (GRPF) plate	Etching	RT	0 to 50,000 (T/C)	3.4 – 26.7	[17]
5	Carbon black/Ecoflex ink on Ecoflex/BTO substrate	Photopolymer extrusion 3D printing	RT	0 to 100,000 (T)	0.39 - 0.62	[18]
6	Silver on polyimide with PMMA encapsulation attached to Kevlar straps	Aerosol jet printing	RT	0 to 60,000 (T)	5.2	[10]
7	Silver on polyimide mounted to polystyrene	Ink jet printing	RT	0 to 3,600 (T)	1.0 - 1.1	[19]
8	Silver on polyethylene, fiberglass, graphite, and alumina	D-W thermal spray and ultrafast laser micromachining	RT	0 to 1,400 (T/C)	0.9 – 21.1	[20]
9	Chromium and copper/gold on polyimide and liquid crystal polymer substrate mounted on steel ribbon	Lithography	22 to 87 °C	0 to 4,000 (T)	1.4 – 2.3	[23]
10	Palladium-chromium on barium strontium titanate dielectric on alumina mounted on GH3536 alloy	Sputtering	Up to 400°C	0 to 2,500 (T/C)	2.05 - 3.4	[21]
11	Silver on polyimide mounted to Al6061 substrate	Aerosol Jet Printing	Up to 300°C	0 to 1,100 (T)	1.0	[24]

2. BACKGROUND

The AM printed strain gauge is composed of layers of multiple materials that make up the packaging of the IDE CSG in this work. As shown in Figure 3, each of the four layers serves a particular purpose and function. For example, the electrically insulative barrier between the metallic substrate and the strain gauge is needed to minimize signal crosstalk and a short circuit from forming between the substrate material and the conductive printed device. The materials for the multi-layered system of the AM strain gauge are chosen to enable testing and operations up to and above 300°C. In selecting the materials for the CSG, the fundamental mechanism that allows the IDE design to measure strain was used to guide the selection. For an IDE CSG, the two mechanisms [25] that can result in a change in the capacitance with mechanical strain include:

1. Changes in electric field near the electrodes due to geometric changes with strain, $\Delta E / E$
2. Changes in dielectric properties of the insulation/encapsulation material with strain, $\Delta\varepsilon / \varepsilon$,

where the total change in capacitance due to strain is:

$$\frac{\Delta C}{C_o} = \frac{\Delta E}{\mathrm{E}} + \frac{\Delta \varepsilon}{\varepsilon} \qquad (1)$$

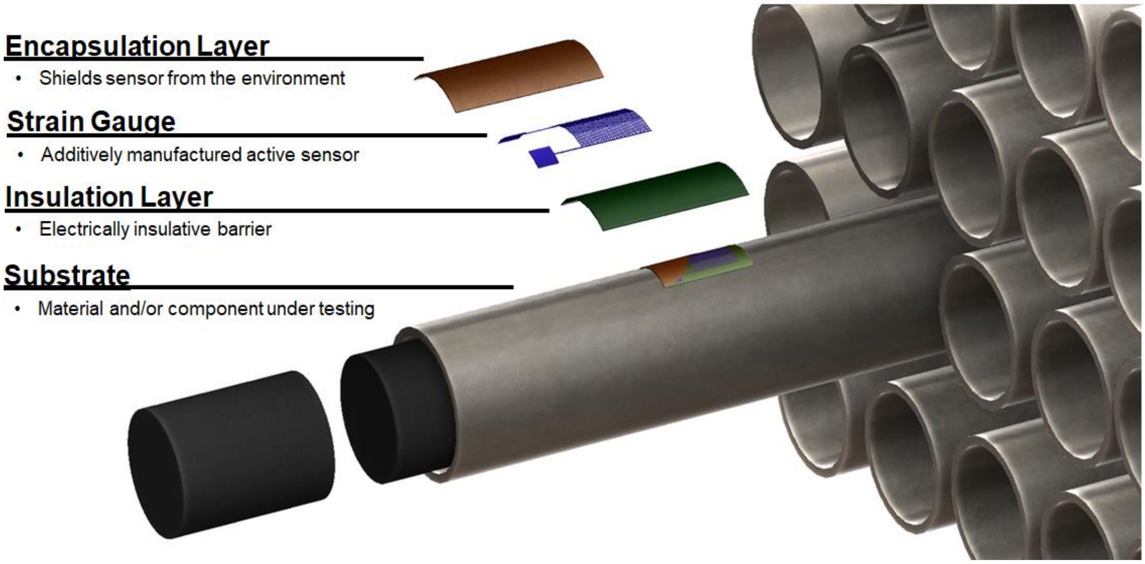

Figure 3. Individual layers of the printed interdigitated capacitive strain gauge on a fuel pin [3].

It can be seen from Eq. (1) that the insulation/encapsulation material used in the CSG needs to allow sufficient deformation (i.e., high ductility) of the IDE design with mechanical strain and/or have dielectric properties that alters when mechanically strained (i.e., dielectrostriction [26]). In addition to these factors, the insulation/encapsulation material must maintain stability in its mechanical and electrical properties at elevated temperatures up to and above 300°C. To help down-select possible candidates for the insulation material, finite element analysis (FEA) using COMSOL Multiphysics was used.

FEA was used to determine the efficiency of strain being transferred from an Al6061 tensile specimen (machined to ASTM E8/E8M [27]) to the surface of the candidate insulation material (i.e., polyimide, silica, zinc oxide, alumina, and silicon carbide). Figure 4 is a two-dimensional cross-sectional view of the model constructed in COMSOL Multiphysics v5.6. In the model, the Al6061 tensile specimen had a fixed constraint on the left end and a boundary displacement of 0.15 mm was prescribed along the y-axis on the right end of the tensile specimen. A 0.15 mm was experimentally and computationally determined to induce an 1100 με in the Al6061 tensile specimen. While strained, a strain transfer ratio (STR) was calculated (Eq. (2)) from the strain observed in the bulk of the Al6061 tensile specimen and top surface of the insulation where the IDE CSG would be fabricated. The STR was calculated for varying thicknesses (i.e., 10-100 μm) of the insulation material. STR is just one index of a strain sensor used to reveal the detection efficiency of a sensing system [28].

$$\%\mathrm{STR} = \frac{\varepsilon_{insulation}}{\varepsilon_{Al6061}} \times 100, \tag{2}$$

where $\varepsilon_{insulation}$ is the strain observed on the surface of the insulation material and ε_{Al6061} is the strain observed in the gauge region of the Al6061 tensile specimen. Figure 5 shows the STR of polyimide, silica, zinc oxide, alumina, and silicon carbide when bonded to the surface of Al6061. A %STR of 100% indicates that the same amount of strain measured in tensile specimen is also seen on the surface of the insulation material. A %STR lower than 100% shows a phenomenon called strain shielding. Although not inherently bad for application where mechanical stress and strain is undesirable, a reduction in %STR affects the strain sensitivity of the IDE CSG. For silica, zinc oxide, alumina and silicon carbide insulation that the amount of strain being transferred from the Al6061 tensile specimen to the ceramic materials reduces with increasing film thickness. This has implications for impeding the strain sensitivity (i.e., gauge factor) of the IDE CSG devices.

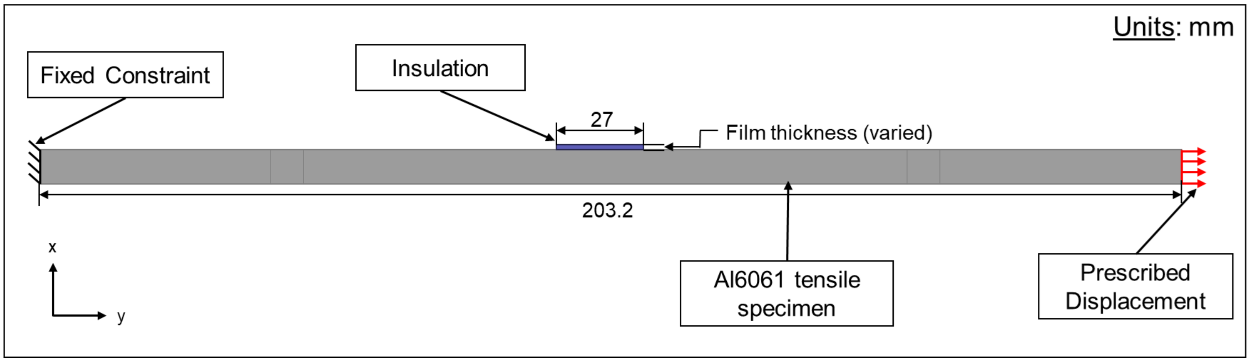

Figure 4. A 2-dimensional cross section view of the COMSOL model's geometry and boundary conditions.

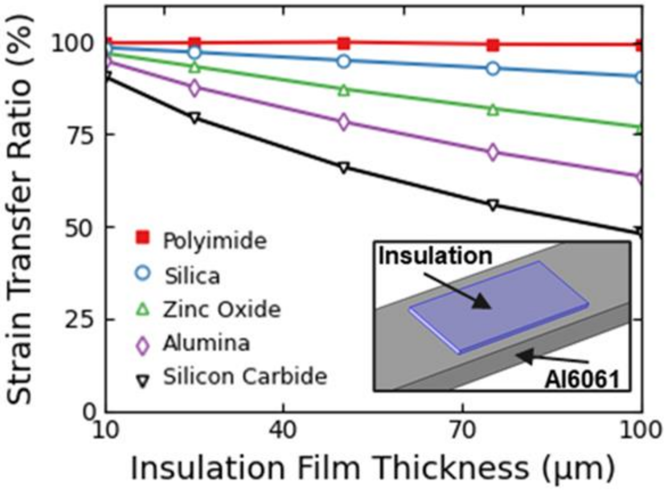

Figure 5. Finite element analysis simulation of the percent of strain transferred from an Al6061 tensile specimen onto the surface of polyimide and ceramic insulation materials at thicknesses between 10-100 µm.

Polyimide, however, has nearly a 100% transferable strain to the surface of the insulation at all thickness between 10-100 µm. Polyimide is also 1) commercially available, 2) electrically insulative, 3) sufficiently ductile, and 4) stable at moderate temperatures (300°C). In addition, it does not exhibit noticeable changes in dielectric properties with temperature [29] or strain. This makes polyimide an ideal insulation material for showing how geometric changes in the electrodes, as a primary mechanism, effects the strain sensitivity of IDE CSG devices up to 300°C. This simplifies Eq. (2) to:

$$\frac{\Delta C}{C_o} = \frac{\Delta E}{\mathrm{E}} \qquad (3)$$

Kim et. al. [11] showed that the change in geometry of the IDE with strain, and therefore the sensitivity of the CSG, is affected by the mechanical properties of the underlying substrate being tested on. This theoretical relation is showed in Eq. (4):

$$\frac{\Delta C}{C_o} = \frac{\Delta E}{\mathrm{E}} = \frac{(1-\upsilon\varepsilon)\cdot(1-\upsilon\varepsilon)}{(1+\varepsilon)} - 1, \qquad (4)$$

where $\boldsymbol{\upsilon}$ is Poisson's ratio of the substrate and $\boldsymbol{\varepsilon}$ is mechanical strain.

3. TESTING OF AM PRINTED STRAIN GAUGES UP TO 300°C

The performance of the IDE CSG are plotted against commercially available bondable resistance based strain gauges (RSG) and the theoretical model described in Eq. (4). The strain gauges were printed using commercial conductive silver nanoparticle ink on an aluminum alloy 6061 (Al6061) ASTM E8/E8M [27] standardized tensile specimens. Al6061 is used as the substrate due to its relevancy as a nuclear material (i.e., cladding material in materials test reactors; [30]). The mechanical and thermal performance of the strain gauges is tested at temperatures between 20 – 300ºC using standardized testing procedures (i.e., ASTM E8/E8M and E251 – 92) [27, 31] to simulate the temperatures found in a traditional light water reactor. Figure 6a compares the experimental results from the RSGs to the expected sensitivity provided by the manufacturer. The manufacturer specified the sensors to have a gauge factor (Eq. (5)) of 2.1 +/-

2.0%; however, the gauge factor from the RSGs were inconsistent and tested well below the uncertainty of the expected sensitivity. Despite being tested under the same conditions at room temperature, the gauge factor varied from 0.55 to 1.58 across three RSG samples (Table 2). This range in gauge factor is due to the manual nature of the application process which can cause variability in the application of the gauge which effects gauge alignment, and final sensor thickness. Successfully bonding free-filament RSGs is known to be cumbersome and require elevated application skills for large structural components [13]. Due to the inconsistent readings, Figure 6a shows that a verification and pre-calibration test will be required after every RSG installation to ensure accurate strain sensing results.

$$\text{Gauge Factor} = \frac{\Delta R/R_0}{\varepsilon} \ or \ \frac{\Delta C/C_0}{\varepsilon}, \tag{5}$$

where R is resistance for RSGs, C is capacitance for the CSGs, and ε is mechanical strain. Figure 6b shows the performance of the CSGs tested at room temperature. The CSGs were fabricated with silver nanoparticle ink using an AJP on a 25 µm thick polyimide tape that was adhered to the gauge length of the Al6061 tensile specimen. The gauge factors of three tested CSGs (Table 2) ranged between 0.97 and 1.30, which were more consistent than the RSGs and demonstrate the repeatability of the AJP process. The experimental CSG data also matched well with the theoretical models described in Eq. (4). This suggests that the changes in capacitance of the IDE CSG under strain are a result of only geometrical deformation and the changing electric field between each neighboring electrode of the IDE structure. Even though the CSGs had a small variance in sensitivity, the measurement uncertainties were higher than the RSGs (as seen from the error bars in Figure 6b). This uncertainty was caused by drifting and measurement instability associated with the internal circuitry of the LCR-meter used for data acquisition [32] rather than the sensors themselves. The change in capacitance when the CSG was strained from 0 to 1100 microstrain was approximately 11.0 fF where the accuracy of the LCR was ±0.22% of the measurement (i.e., ±26.75 fF for CSG-1).

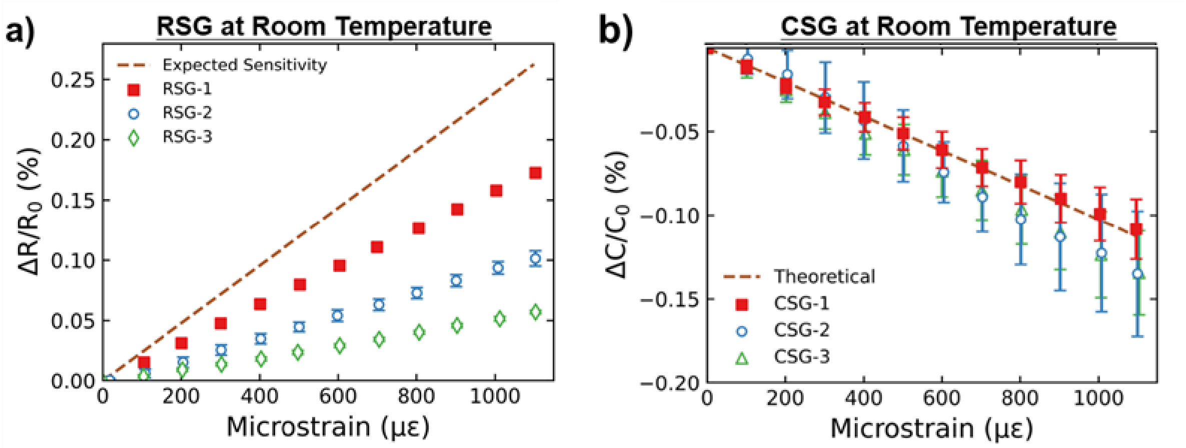

Figure 6. In-situ strain sensitivity measurements of three different a) commercially available RSGs and three different b) silver ink AJP printed CSGs for a total of six devices (Table 2) in a room temperature environment were obtained from seven strain cycles during mechanical testing for each sample.

Table 2. Summary of the initial readings and gauge factor of the six total devices (three RSG and three CSGs) tested during the room temperature experiments. The gauge factor was calculated using the experimental results shown in Figure 6.

Sample ID	Initial Resistance (R_0) or Capacitance (C_0)	Gauge Factor at Room temperature
RSG-1	136 Ω	1.58
RSG-2	127 Ω	0.96
RSG-3	132 Ω	0.55
CSG-1	12.16 pF	0.97
CSG-2	9.99 pF	1.21
CSG-3	10.36 pF	1.30

The sensitivity of an RSG and CSG on Al-6061 were evaluated from room temperature to 300°C at 100°C intervals. At temperatures above 100°C, the maximum amount of mechanical strain imposed on the Al6061 substrate was reduced to approximately 400 microstrain for 200°C and 300°C testing to prevent exceeding the elastic limits of Al6061 and plastically deforming the substrate [33]. The strain sensor signals demonstrated sensitivity to strain even at elevated temperatures; however, the signals had reduced linearity and increased variability in the gauge factor. Figure 7 shows the results of strain induced on both the RSGs and CSGs. Between 25°C and 200°C, the RSGs had a gauge factor of 1.52 – 1.58 with low margins of error (Figure 7a). At 300°C, the RSG data began to lose linearity; however, the gauge factor comparatively stayed the same at 1.54 (Table 3). The printed CSGs (Figure 7b) had a gauge factor of 0.97 and 1.08 at room temperature and 100°C, respectively. At 200 °C and 300 °C, the CSGs gauge factor increased to 1.87 and 1.68, respectively. The changes in sensitivity and larger errors at temperatures above 200°C can be attributed to the compromised mechanical properties of aluminum alloys at temperatures above 200°C [34]. More specifically, the tensile yield strength of Al6061 significantly decreases from 282 MPa to 31 MPa as temperature increases from 22°C to 300°C [33] due to thermal annealing of a Al6061-T6 to an -O. To further verify that the change in of the CSG is a result of the substate material and not the sensor design, the IDE was fabricated on stainless steel 316L (SS316L). Figure 7c shows the results of the IDE CSG that was fabricated on SS316L and tested from room temperature to 300°C at 100°C intervals. The CSG printed on SS316L had a more consistent gauge factor than a CSG with similar geometry on Al6061 since SS316L does not exhibit an abrupt change in its tensile yield strength over this temperature range. Between room temperature and 300°C, the gauge factor had a range between 0.85 and 0.90. Despite the difference in the Poisson's ratio of Al6061 and SS316L (Figure 8), the IDE CSG continued to match well with the theoretical models described in Eq. (4).

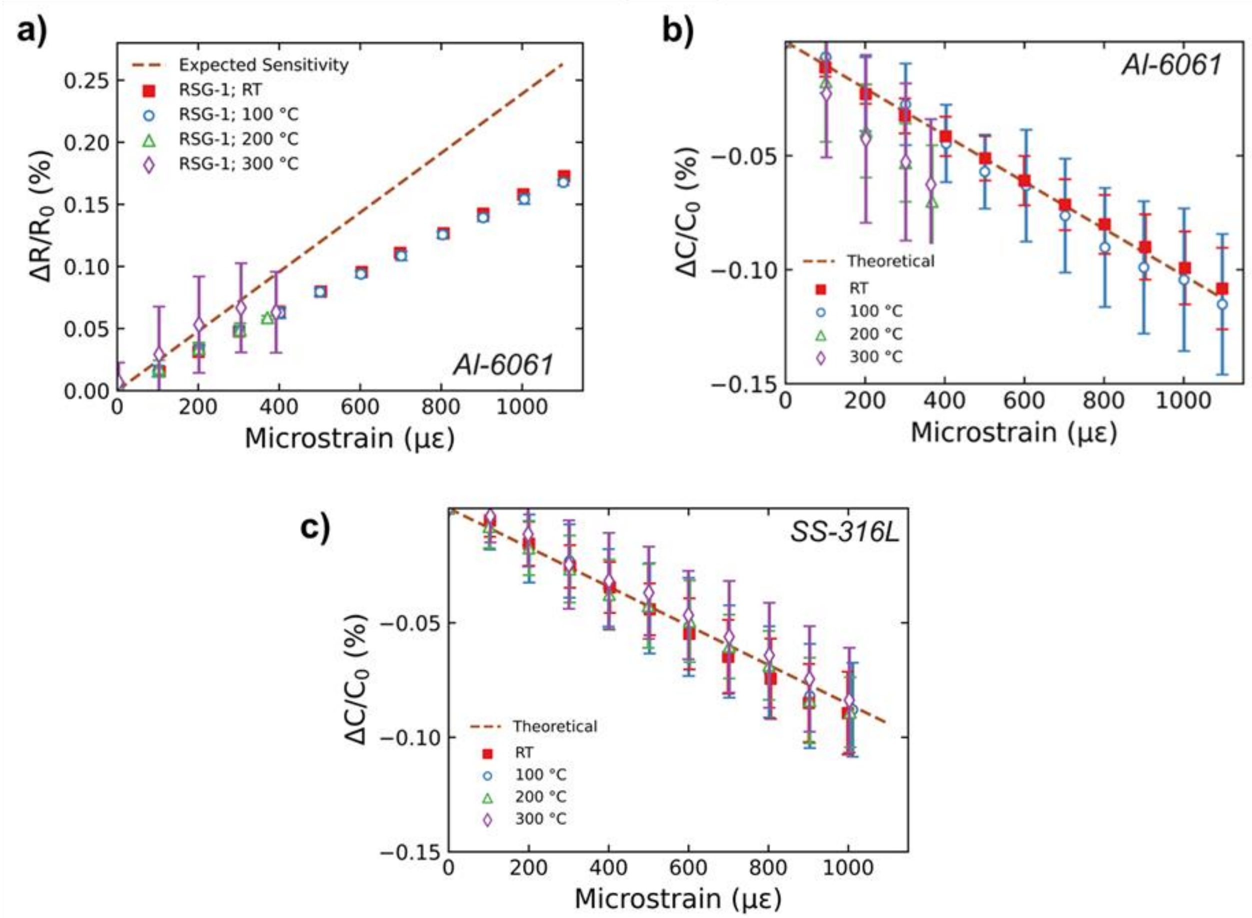

Figure 7. In-situ strain sensitivity measurements were collected from room temperature up to 300°C of an a) RSG on Al6061 substrate and printed CSGs on b) Al6061 and c) SS316L substrate. Results of all three devices are summarized in Table 3.

Table 3. Summary of the initial readings and gauge factor of an RSG and two CSGs devices and one RSG (RSG-1) tested from room temperature to 300°C. The gauge factor (Eq. (5)) was calculated using the experimental results shown in Figure 7.

Sample ID	Initial Resistance (R_0) or Capacitance (C_0)	Room Temperature	100°C	200°C	300°C
RSG-1 on Al-6061	136 Ω	1.58	1.53	1.52	1.54
CSG on Al-6061	12.16 pF	0.97	1.08	1.87	1.68
CSG on SS-316L	12.58 pF	0.95	0.90	0.89	0.85

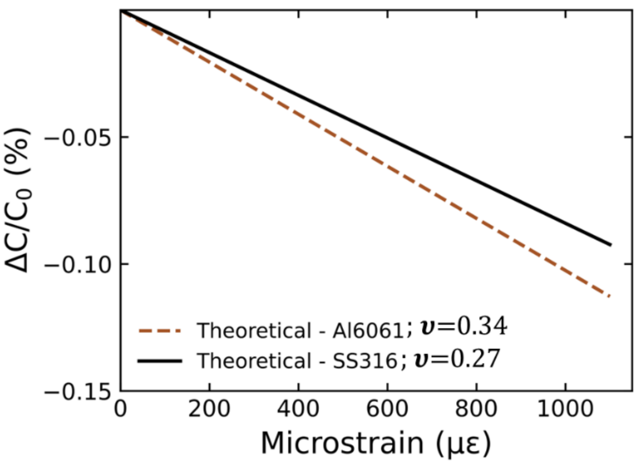

Figure 8. Theoretical performance of the IDE CSG on Al6061 and SS316 using Eq. (4).

4. DEVELOPMENT OF AM PRINTED STRAIN GAUGES UP TO 500°C

The polyimide tape insulation and encapsulation discussed in Section 2 becomes unsuitable for operation above 300°C due to the thermal degradation of the silicone adhesive used with the polyimide film. To enable the application of printed IDE CSGs for higher temperature applications beyond 300°C, a commercially available silica-based printable insulation (QQ550, DuPont) was initially investigated as a possible insulation and encapsulation material. The ideal material would be inorganic (e.g., ceramic), and have a high electrical resistivity, sufficiently ductile, and high dielectric constant. Initially, commercially available paste materials were procured from DuPont and used as a potential candidate for printable insulation material. With the silica-based ceramic cement, it was found that the methods (i.e., screen printing) for manually applying the insulation layer (Figure 3) resulted in surface topography that was rough and had surface defects (i.e., pin holes, porosity) that caused discontinuity in printed sensors (Figure 9). This conventional method of application was performed by taping off a region of the substrate to create a reservoir, drop casting a pool of cement material on one edge of the tape, and then using a razor blade to scrape an even layer of ceramic cement material across the region of interest. Even though it was shown that with practice and a post-polishing step that the layer can become smooth (i.e., average surface roughness, Ra = 1.5µm) and thin (i.e., thickness, h = 30µm), there were still challenges with consistency in application and surface defects. These inconsistencies in surface quality and film thickness affect the performance and reliability of the capacitive strain sensor. The application and challenges of using AM to fabricate multiple layers have also been previously discussed [35-37].

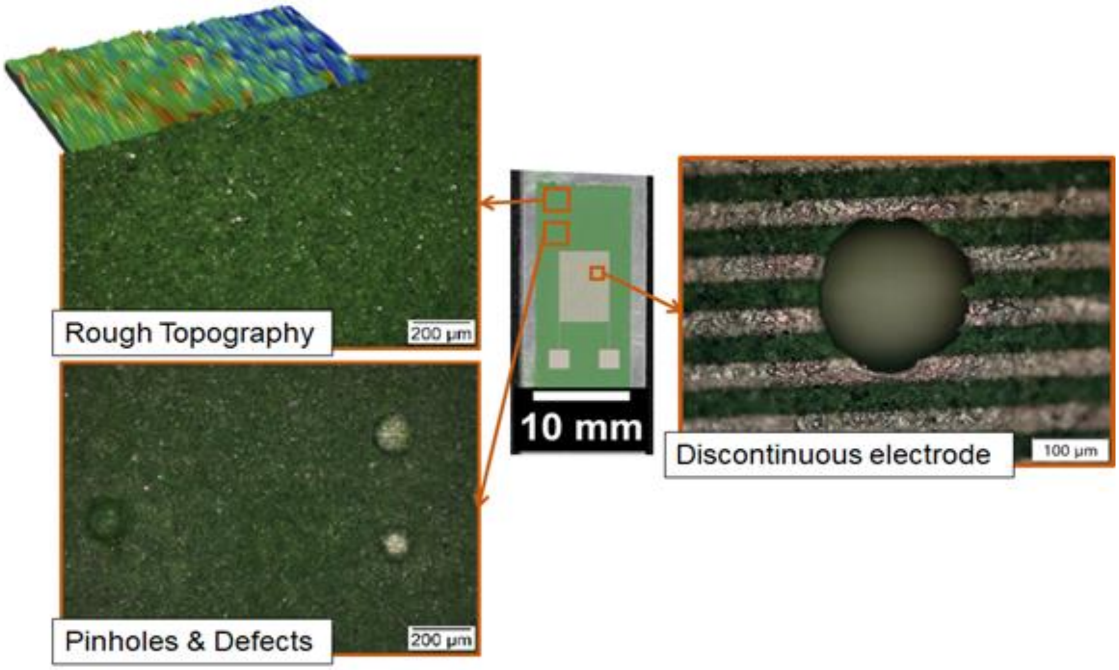

Figure 9. Ceramic cement has rough surface topography and defects that are detrimental to the performance of printed capacitive strain gauges.

To mitigate the issue with inconsistent fabrication and unfavorable rough surface topography of the insulation layer, an additional AM printer (Voltera V-One) was implemented into the fabrication process. The Voltera V-One printer is a desktop extrusion-based printer that deposits a viscous paste material onto a flat surface by mechanically pushing a piston in the printer cartridge, which drives material out of a fine tipped nozzle. Using the Voltera V-One printer allowed for tighter tolerances in film roughness and thickness when compared to the manual application method (Figure 10). Upon visual inspection, the printed electrodes of the CSG also had a morphology that was more uniform across the whole surface area of the sensor on the Voltera V-One printed insulation surface when compared to the manually applied insulation surface.

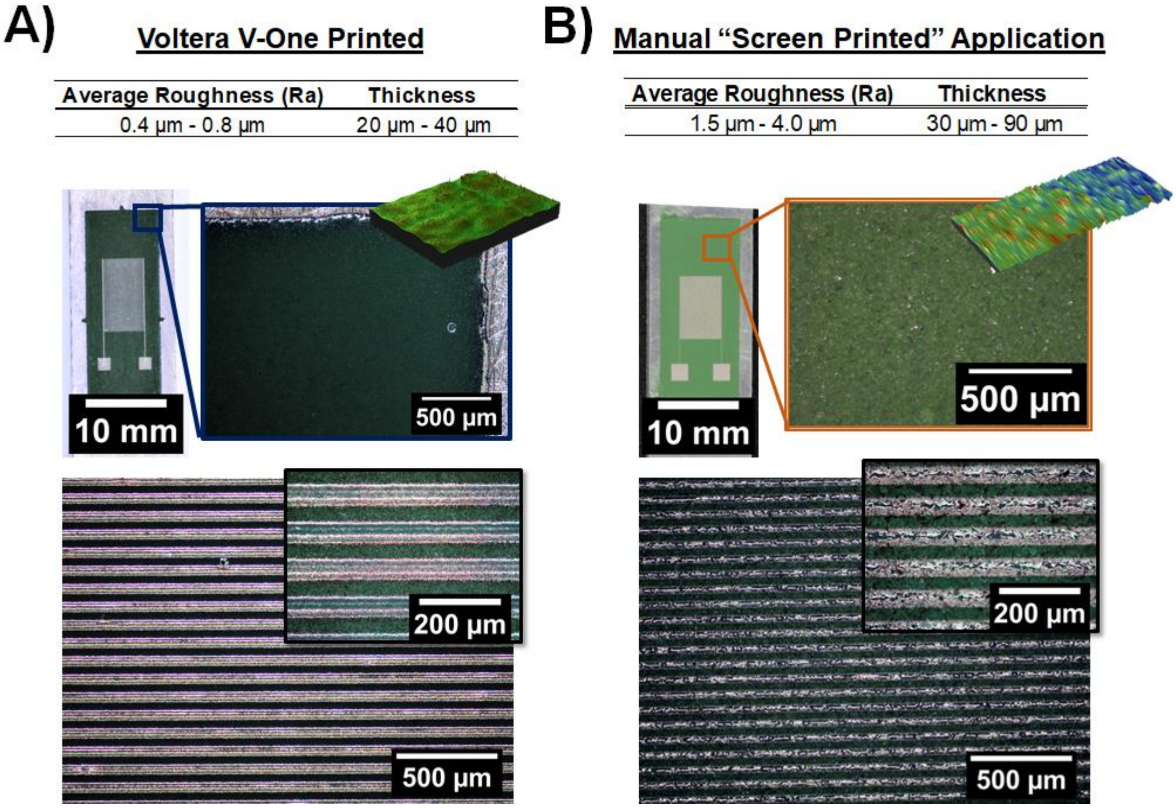

Average Roughness (Ra)	Thickness
0.4 µm - 0.8 µm	20 µm - 40 µm

Average Roughness (Ra)	Thickness
1.5 µm - 4.0 µm	30 µm - 90 µm

Figure 10. A table of average roughness and insulation thickness, as well as optical images of the surface and printed electrodes on: A) Voltera printed silica-based insulation (i) and B) manual screen-printed ceramic cement.

Even though the Voltera V-One printer allowed for better control with fabricating the insulation layer for the AM CSG system, the stiffness (i.e., low ductility) of the cured silica-based ceramic insulative film, coupled with the thickness, prevented mechanical strain experienced by the aluminum substrate from efficiently being transferred to the IDE CSG. This strain shielding effect was previously discussed and showed with FEA (Figure 5). To experimentally show the reduction in the transferred strain, digital image correlation was used to show the strain on a printable silica-based insulation material on the Al6061. Figure 11 shows that the strain observed on the surface of the insulation was 500 microstrain while the strain on the Al6061 substrate was 800 microstrain. This resulted in a 63% strain transfer from the substrate to a 30 µm thick insulation. As discussed in Section 2, the performance of the IDE CSG is a result of a change in geometry of the IDE design and/or a change in properties of the dielectric material (i.e., insulation/encapsulation layer) of strain gauge (Eq. (2)). Since most insulative ceramics materials are inherently stiff and therefore a low STR, the dielectrostriction effects (i.e., change in dielectric constant with an induced stress) of the materials are investigated. The dielectric constant of silica was observed to increase with mechanical tensile strain [26], however the composition of the silica-based paste used in this work was found to have only a relatively small and statistically irrelevant changes in the capacitance with strain. Although the ability to print the insulation material with sufficient consistency and a relatively smooth surface topography, it was found that low STR and relatively small changes in dielectric constant makes the silica-based insulation film not conducive for the IDE CSG design. Another candidate material that was observed to have a change in dielectric constant with mechanical strain is barium strontium titanate (BST) [21, 38], however this material currently is not available for purchase in a printable form from a commercial vendor. This required the formulation of BST into an AM printable ink/paste.

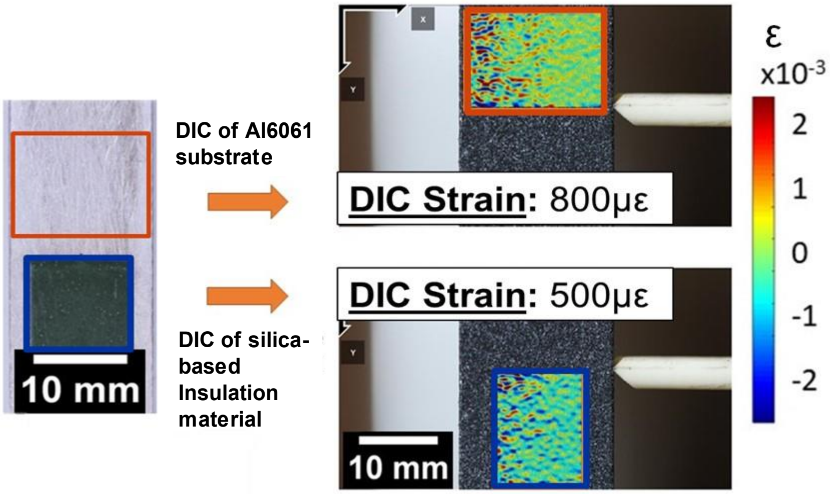

Figure 11. Digital image correlation (DIC) experimentation of the strain observed in the Al6061 and the printable silica-based paste material.

BST films have been widely integrated into novel microelectronic systems such as capacitors, microwave chips, microsensors, and radio frequency microelectromechanical (MEMS) devices owing to their high dielectric constant and highly tunable dielectric properties [39-41] Despite their widespread use, however, very limited data exist on the mechanical/ elastic properties of printed BST films. Mechanical properties of BST reported in the literature include those for thin film BST deposited on substrates using radio frequency magnetron sputtering [42] or bulk BST synthesized using solid state reaction [43]. There is considerable scatter in the elastic properties reported between these studies. The lack of reliable data on the elastic properties of BST, particularly for printed BST films, precluded us from performing analyses of strain transfer ratio as a function of film thickness using finite element methods for the BST film, as was done for other candidate insulating materials. Nevertheless, to enable its application as an insulation/encapsulation layer for the IDE CSG, BST nanoparticles (US Research Nanomaterials, Inc.) were purchased and used to formulate a printable paste material using the Voltera V-One printer. This was achieved by grinding the nanomaterial in a mortar and pestle and then mixing in ethylene glycol until a paste-like consistency was achieved. Initial formulations included three different batches at 90 wt%, 85 wt% and 80 wt% particle loading. The paste was mixed in a centrifugal mixer (Thinky Corporation; ARE-310) at 1500 rpm for 30 seconds and then 2200 rpm for 30 seconds for 3 cycles until a uniform consistency was achieved. It was found that the 90 wt% particle loading BST paste deposited without clogging the printer's nozzle. Figure 12d shows a representative image of a printed BST pad.

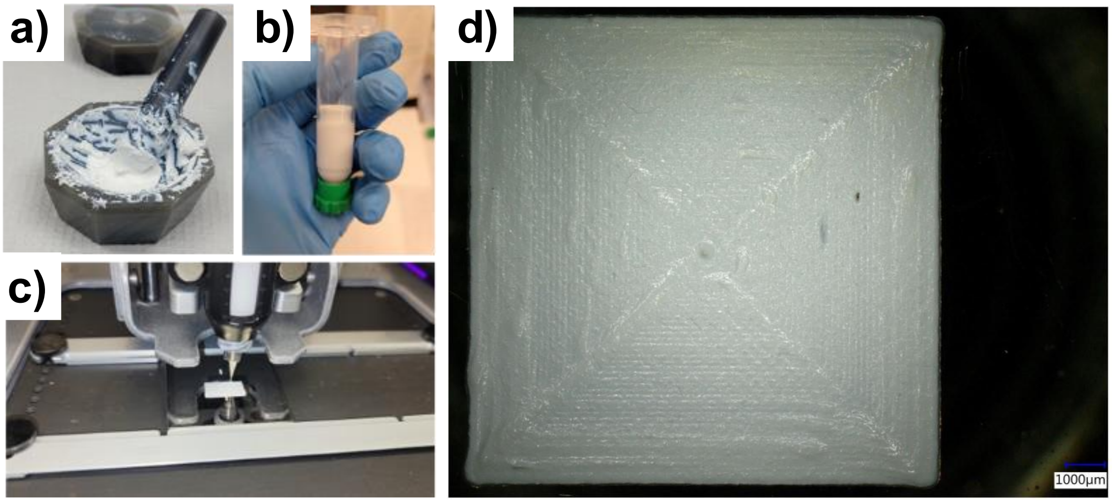

Figure 12: Sequential photos that show the formulation of the ink to a printable pad. a) barium strontium titanate nanoparticles were ground and mixed in an ethylene glycol solvent to allow for a 90 wt% particle loading, b) mixed material was loaded in a printer ink cartridge and then c) used to print on the Voltera V-One printer. d) A representative photo of the Voltera printed barium strontium titantate pad.

The thickness of the Voltera printed BST film was measured to be approximately 135 µm – 300 µm using laser profilometry. In addition to the coefficient of thermal expansion (CTE) mismatch between the BST and SS316 substrate, the thickness of the film causes cracking in the film (Figure 13a). Cracking in printed films are deposition, drying and sintering is a common issue [44, 45] that can be mitigated. While printing, the film thickness is affected by the rheological properties of the ink/paste and is also not an easily controllable with the process parameter on the Voltera V-One. To show that the film thickness of BST reduces observable crack formation, Figure 13b shows the resulting BST film after being applied with the manual screen-printing technique discussed earlier. The BST was applied onto the substrate by using a 25 µm thick polyimide tape as a temporary square dam/stencil and then using a flat edge to scrape a uniform layer of BST material across the surface. Current on-going efforts, however, are supporting the formulation and testing of aerosol jet printed BST films, which will allow for the deposition of thinner films. Figure 14a shows the initial BST that successfully formulated to print with the aerosol jet printer. The AJP printed film was thinner than the film that was screen printed (Figure 13b), however had visible variations in the thickness (i.e., 2-20 µm) of the film due to the process drift that can occur during the AJP fabrication process for large area prints (i.e., > 100 mm^2) [24]. Figure 14a illustrates the non-uniform thickness across the BST film printed using AJP.

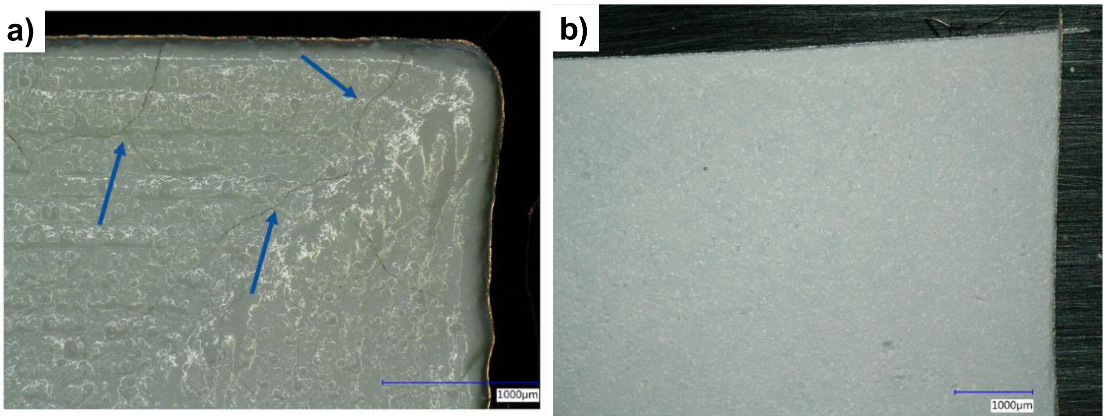

Figure 13. a) Cracking in the 135 µm thick Voltera printed barium strontium titanate film due to thickness and thermal expansion mismatch. b) A 55 µm thick barium strontium titanate film that was screen printed with no visible cracking.

Formulation of a successfully printed BST ink that can be used with the AJP was guided by previous work where low-temperature sinterable BST was demonstrated [46]. The formulation of BST ink for the AJP was driven by the need to mitigate: 1) cracking that is initiated by a CTE mismatch between BST and substrate at elevated temperature and 2) AJP process drifting that causes non-unform deposition. To help alleviate these challenges, varying amounts of dispersant (i.e., ammonium polymethacrylate) and co-solvent (i.e., 1-Methoxy-2-propanol) was added to the BST/ethylene glycol paste previously formulated for the Voltera V-One. Adding additional immiscible co-solvents to the ink enhances the drying rate and particle cohesion [44] of the deposited film which can reduce the cracking. To promote consistent deposition with the AJP, the BST ink was continually stirred using a magnetic stir bar to keep the ink evenly dispersed and homogenous through the printing process. In addition, a solvent bubbler was used to flow saturated carrier gas through the AJP process to mitigate evaporation of the high vapor pressure solvent (i.e., 1-Methoxy-2-propanol) in the BST ink. This improvement in the ink formulation and fabrication process resulted in a BST film that had a uniform, 7 µm thick print across the whole film (Figure 14b) after sintering in air at 600°C for 3 hours. Figure 14c shows a representative scanning electron microscopy (SEM) micrograph of the BST film after sintering at the same conditions. Although the BST nanoparticles appear to be fused into larger-scale aggregates, considerable porosity was observed in the morphology of the printed film.

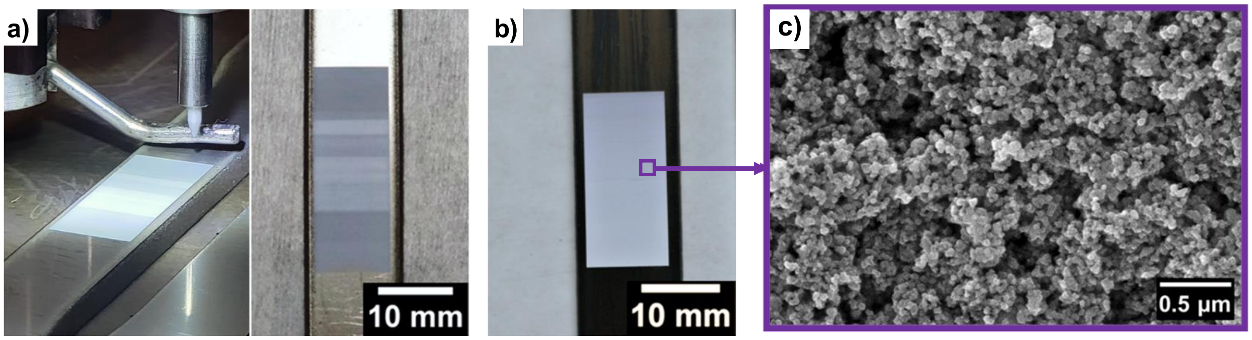

Figure 14. a) Initial formulated barium strontium titanate ink material that was printed with the aerosol jet printer showed non-uniform and inconsistent deposition. b) Improved AJP process controls allowed for the deposition with more uniform film thickness of 7 µm across the whole printed film. c) scanning

electron microscopy micrograph of the BST films porous microstructure after being cured in air at 600°C for 3 hours

As previously mentioned, the AJP technique provides versatility in its ability to fabricate on substrates with both planar and non-planar surfaces. Figure 15 demonstrates the ability to additively print IDE CSGs with polyimide and BST insulative layers on both flat and cylindrical substrates. The fabrication of these IDE CSGs was not previously possible with conventional fabrication techniques (i.e., photolithography) and certain direct-write additive technologies (i.e., Voltera.V-One). The ability to fabricate on curved specimens is of interest for printable strain gauges as similar geometry materials are commonly encountered in structural components of reactors.

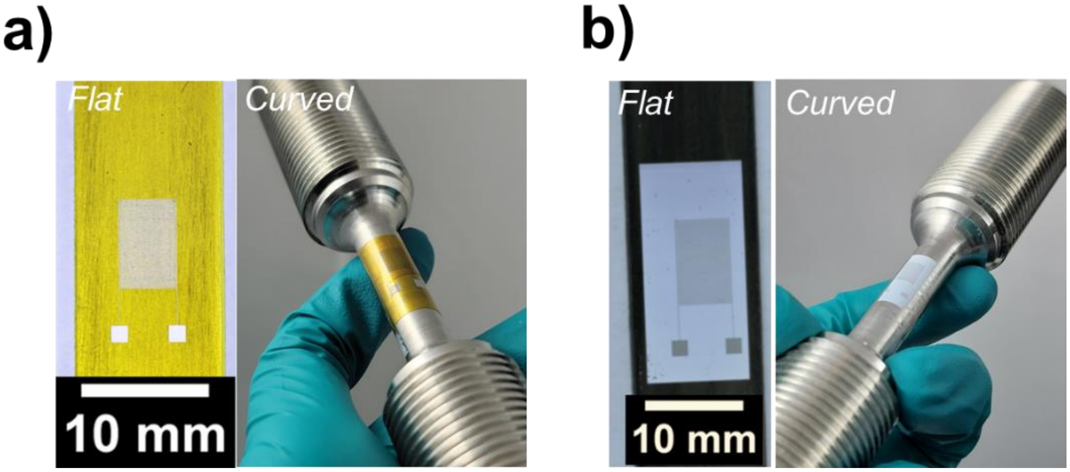

Figure 15. CSG printed on a flat and cylindrical tensile specimen on both a) polyimide and b) barium strontium titanate insulation material using an aerosol jet printer.

To test the dielectric constant of the BST film, a dielectric tester that is outfitted with a Keysight E4980A LCR-meter in a furnace was used (Figure 16a). This allows for the dielectric constant measurement of four samples simultaneously with temperatures up to 800°C. These measurements are performed between two platinum electrodes as shown in Figure 16b. Due to the configuration of the dielectric tester and the fabricated sample, the effective dielectric constant of both the BST film and 1 mm thick SS316 substrate was measured jointly. The dielectric constant was measured for: 1) five thermal cycles from room temperature to 500°C and 2) a five-hour dwell at 500°C.

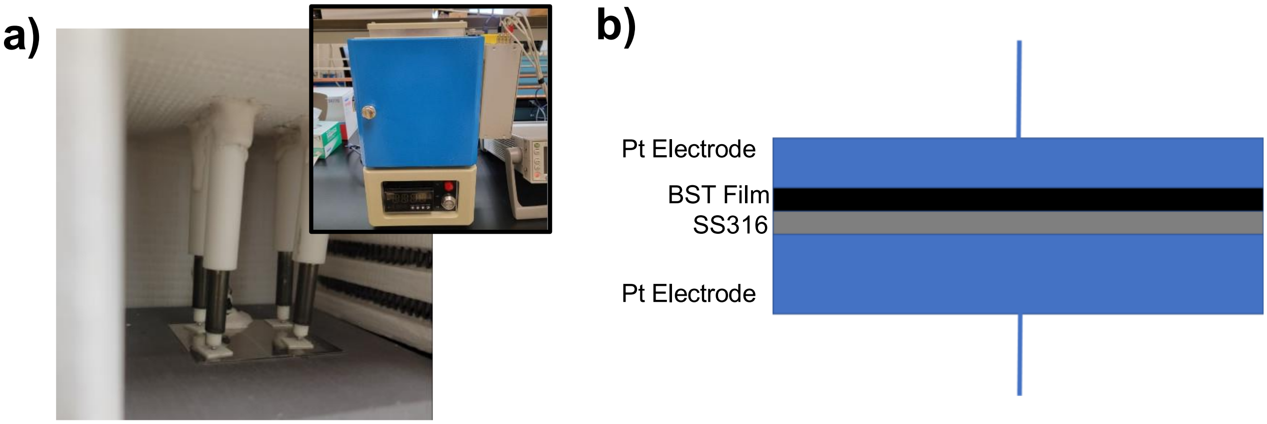

Figure 16. a) Furnace setup that is outfitted with a Keysight E4980A LCR-meter for measuring dielectric constant of four thin films simultaneously up to 800°C. b) schematic of the relative position of the platinum electrodes and the materials dielectric properties that are measured in the set-up.

Figure 17 shows the effective dielectric constant of barium strontium titanate on SS316L as temperature is ramped up to 500°C for five separate thermal cycles from room temperature. These measurements were also collected at different frequencies between 1000 Hz and 1 MHz (Figure 19). The temperature-dependent, effective dielectric constants exhibited a maximum value at ≈ 24°C. This feature in the temperature dependence of the dielectric constant occurs at the Curie temperature (T_c) [47]. Figure 19 shows that the effective dielectric constant decreases with increasing frequency. There is an observed peak in the measured effective dielectric constant at room temperature (24°C) due to a polymorphic transformation of BST at T_c. Below the Curie temperature, BST has a tetragonal crystal structure and gives BST ferroelectric characteristics. Above the Curie temperature, BST has a cubic crystal structure and has paraelectric characteristics. It was found that stress in the BST film causes a change in the permittivity measured through the film while in the paraelectric phase [38]. Also shown in Figure 17, the dielectric peak increases after the first three runs, however, drops in magnitude during run 4 and run 5. This drop in effective dielectric constant is attributed to the damages to the BST film (Figure 18) caused by the platinum electrode during thermal cycling. The dielectric constant could also be affected by the changing interface of the substrate film, film thickness, microstructure, surface morphology, and/or residual stresses in the film. These factors have implications for affecting the performance of the IDE CSG while exposed to high temperature and other harsh environment conditions (i.e., irradiation, etc.).

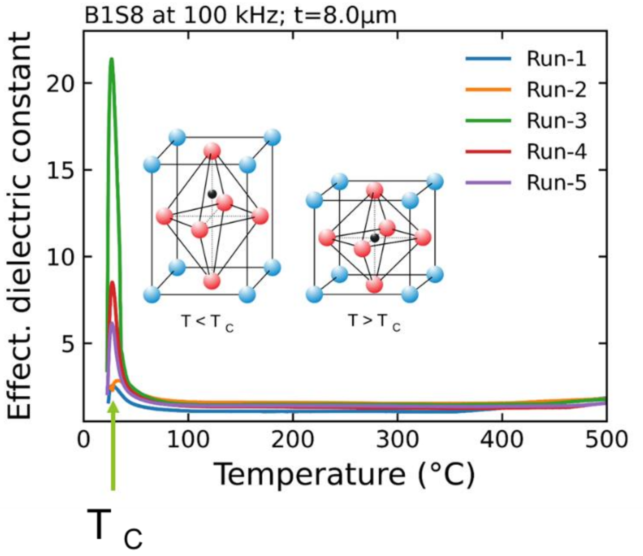

Figure 17. The effective dielectric constant of barium strontium titanate on SS316L as temperature is ramped up to 500°C for five thermal cycles. There was a peak in the measured dielectric constant at room temperature (24°C) due to a polymorphic transformation at the curie temperature (T_c).

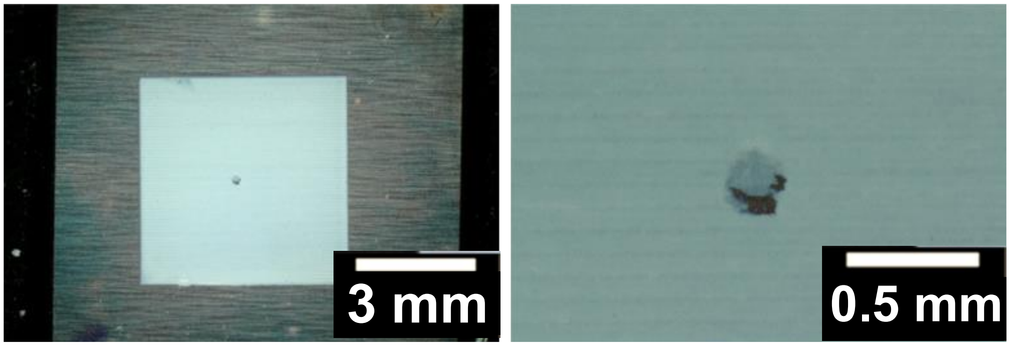

Figure 18. Damage to the barium strontium titanate film from the Pt electrode on the dielectric tester after ramping up to 500°C for five thermal cycles.

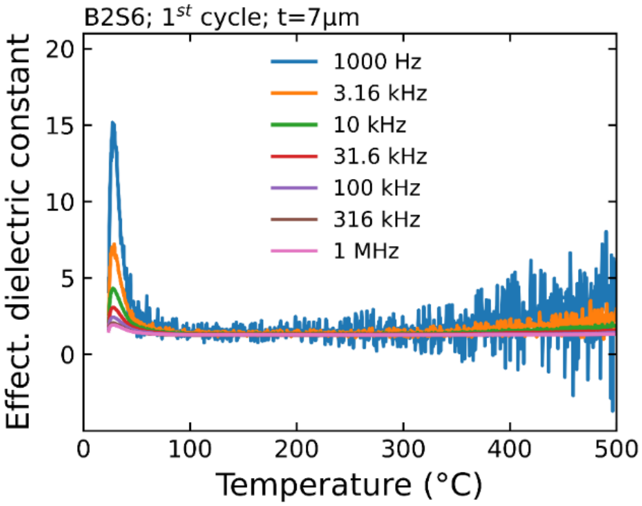

Figure 19. The effective dielectric constant of barium strontium titanate on SS316L as temperature is ramped up to 500°C. The dielectric constant was measured at different frequencies between 1000 Hz and 1 MHz.

Figure 20 shows the effective dielectric constant of the AJP printed BST film on SS316L during a five-hour dwell at 500°C. The dielectric constant maintains stability throughout the five-hour thermal dwell. The stability of the dielectric constant of BST at 500°C is a promising result as it allows for the measurement of mechanical strain without the dielectric constant drifting/changing which causes measurement error.

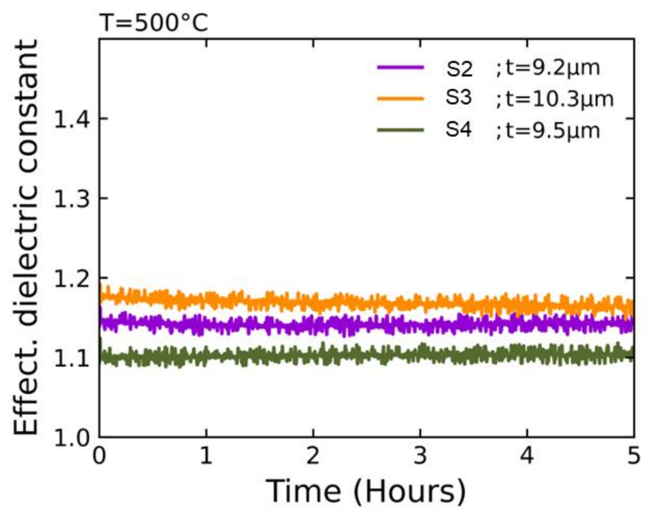

Figure 20. The effective dielectric constant of barium strontium titanate on SS316L during a 5-hour dwell at 500°C.

The performance of the AJP printed CSGs while tested at 22°C on BST insulation is shown in Figure 21a. The initial capacitance of the IDE was 445 pF, which is an order of magnitude higher than the CSGs with polyimide insulation/encapsulation. The gauge factor of the CSG on BST however, was calculated to be 0.2 which is lower than the gauge factor of the IDE CSGs with polyimide insulation (Table 2). Since the CSG was measured below the Curie temperature, the BST film was measured in ferroelectric phase and not the paraelectric phase where stress was found to reduce the permittivity of BST film [38]. In addition, the BST film is porous and has micron-scale cracks (Figure 22) that made it a challenge to reliably measure strain and maintain continuity at 500°C and are attributed to fluctuating capacitance readings and large errors (Figure 21b). As seen in Figure 21b, the CSG tested at 500°C does not correlate with mechanical tensile strain and has a calculated gauge factor of approximately 0.01. At about 700 microstrain, one of the two lead-wires used to connect to the CSG detached from the contact pad of the sensor causing the CSG to lose signal. Currently, silver epoxy is used to bond individual lead wires to the printed IDE CSG since it is easiest to implement and the most common technique to integrate to AM sensors [11, 17, 20, 48]. A known limiting factor of AM sensors is the development of appropriate interconnection that can maintain reliable electrical and mechanical performance in harsh environments [49-52]. The challenge to minimize signal noise is exacerbated by external parasitic capacitance and the limitations of the LCR-meter used for data acquisition (discussed in *Section 3*). The interconnection of the lead wire to the CSG is currently an on-going challenge for reliable long-term measurement of the printed CSGs on BST insulation at elevated temperature. In addition, current efforts are also investigating methods to reduce porosity of the BST film and/or minimizing the cracking in the film that is caused from the CTE mismatch between the BST and SS316L at elevated temperatures.

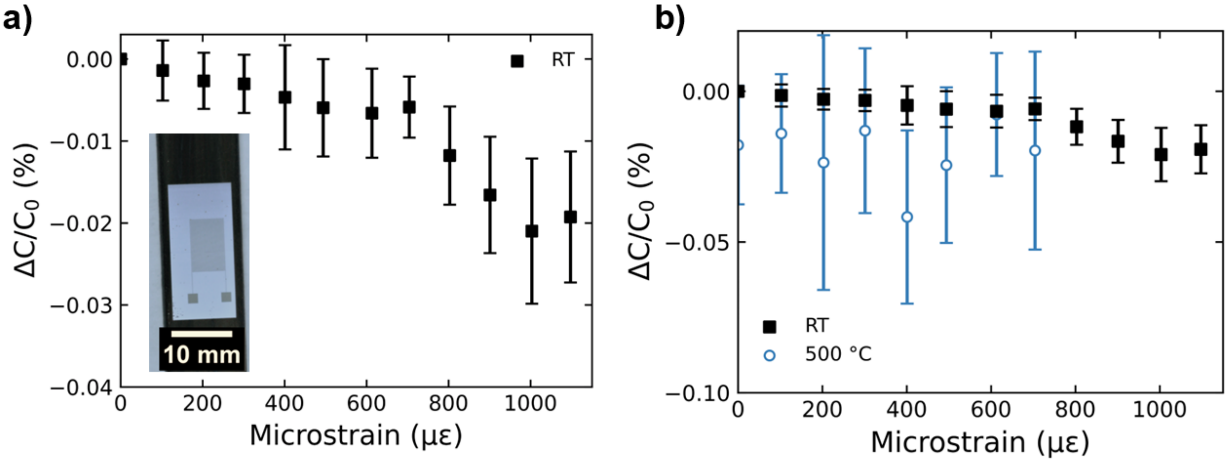

Figure 21. In-situ strain sensitivity measurements of AJP printed CSGs with BST insulation tested at a) room temperature and b) 500°C with the results from room temperature overlayed. The inset image on (a) shows a representative CSG that was fabricated on BST. Error bars were obtained from seven strain cycles during mechanical testing for each sample.

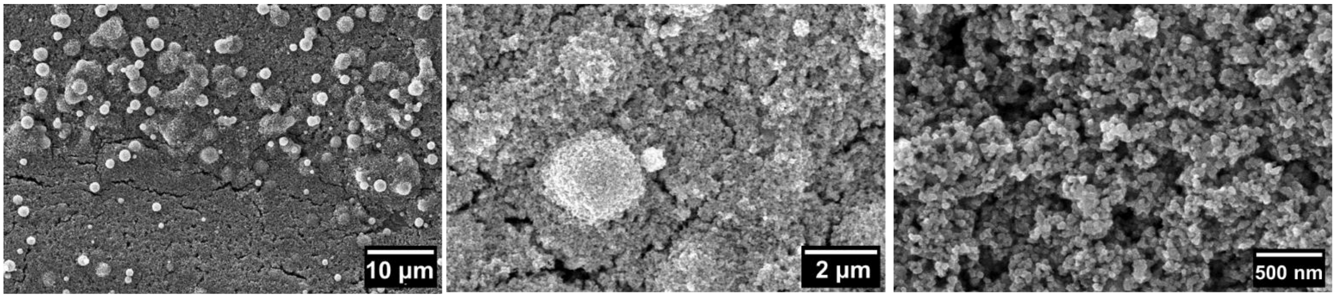

Figure 22. Scanning electron microscopy image of the barium strontium titanate film after curing the print at 600°C for 3 hours.

5. DEVELOPMENT OF QUALITY CONTROL METRICS FOR TESTING THE ROBUSTNESS AND RELIABILITY OF AM PRINTED STRAIN GAUGES

5.1 Tape Adhesion Testing

In order to characterize the resiliency of the printed structure on metallic surfaces, the adhesion strength was characterized. Test methods outlined by ASTM Standard D3359-09 (Appendix B) for measuring the adhesion of coating films on metallic surfaces was used. This standard requires the application and removal of a pressure- sensitive tape over cross-hatched cuts that are made in the film. The standard uses visual inspection of the cross-hatched grid for any removal of ink after the tape has been pulled off. The standard grades the affected area based on how much of the ink/coating detached from the metallic substrate. As seen in Figure 23A, a Shimadzu materials testing system was used to pull the tape off the printed specimen at a steady rate.

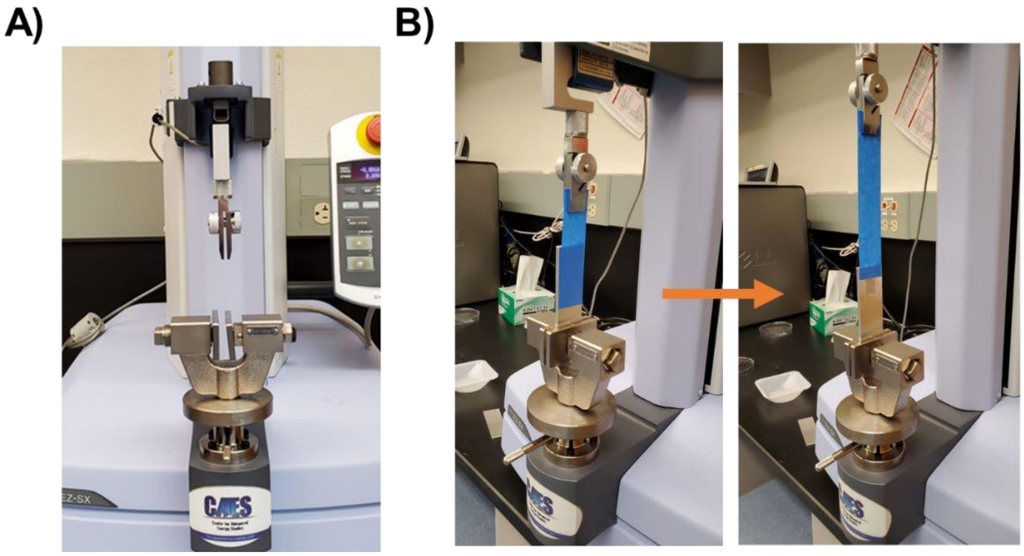

Figure 23. A) Shimadzu Materials Testing System with grips for adhesion testing B) Frame-by- Frame image of how tape is pulled off the test specimen.

In Figure 24, the force required to pull-off two tapes with different certified and adhesion characteristics (i.e., blue and beige pressure sensitive 3M Scotch® tape) were tested on clean, bare Al6061 substrates to validate the baseline strength of the tapes. The beige tape required approximately 10 N of force to pull the tape off and the blue tape required approximately 2 N of force.

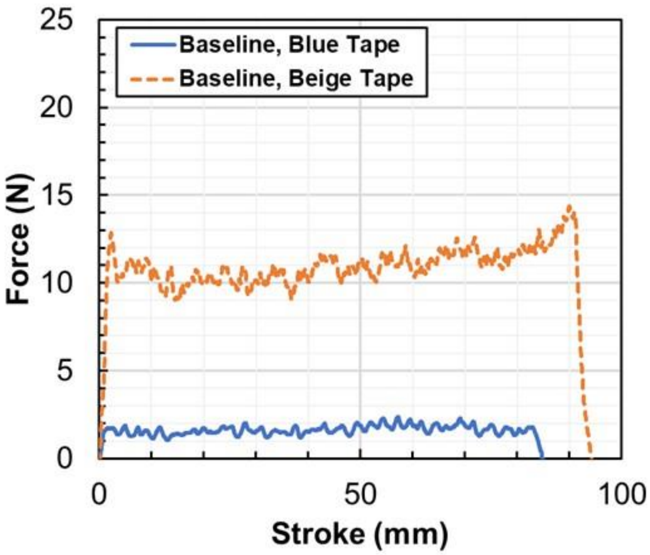

Figure 24. Baseline adhesion strength of a blue and beige pressure sensitive 3M Scotch® tape on bare Al6061

In this preliminary adhesion testing using the tape testing method, the cross-hatching pattern required by the ASTM standard was printed directly on the Al-6061 substrate using silver ink. Figure 25A shows the force required to pull off the tape from Sample A and Figure 25B shows the residue that adhered to the tape prior to testing with the blue and beige tape. It is evident that the force required to peel the tape over the printed cross-hatched pattern is ≈8 N higher than the corresponding peeling force over the bare Al-6061 substrate. As seen in Figure 25B the blue tape detached very minimal amounts of printed ink. The beige tape detached a substantially more amount of ink from the surface as shown by the arrow in Figure 25B and Figure 26. Figure 26 shows the printed structure pre- and post- adhesion testing. The results from this test were found to be limited because adhesion performance was graded based on a visual inspection of the percentage of ink removed after the tape has been pulled off and provided no quantitative data. It should be noted that the ASTM D3359 tape test is better suited for ranking the adhesion performance of samples based on visual assessment, as opposed to providing a quantitative measure of adhesion strength. The limitations/ challenges associated with quantifying adhesion using the tape test (ASTM D3359) have been noted in the literature [53]. These include the lack of specified pressure during the application of tape over the sample and absence of a specified peel rate. To mitigate the limitations of the tape test, a standardized pull-off adhesion test and developmental laser-induced spallation technique discussed in the next section was used for quantitative pull-off adhesion measurements.

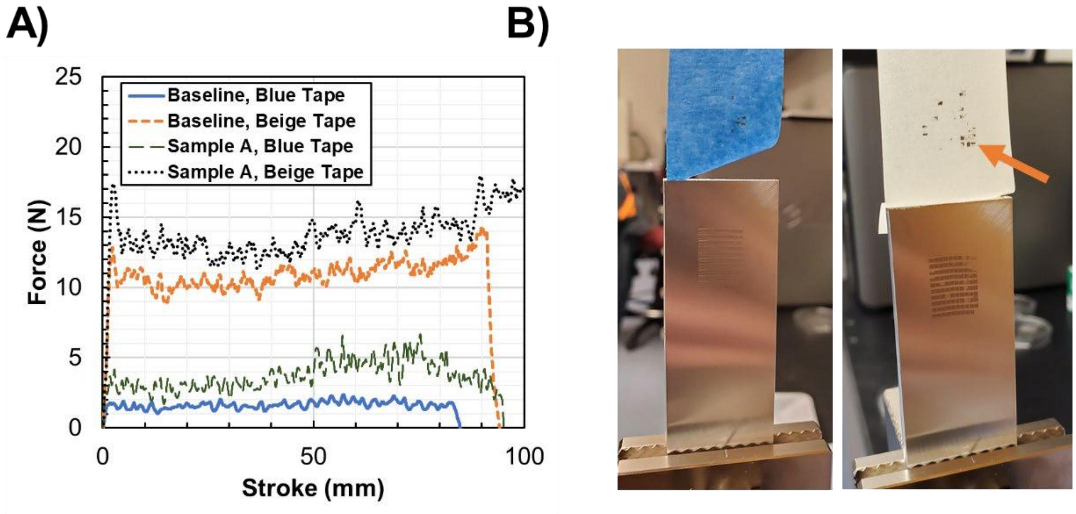

Figure 25. Sample A was printed with a cross-hatch pattern and did not require cuts with special tooling: A) Force vs Stroke distance data of Sample A, B) Residue on the tape after testing Sample A with a blue and beige pressure sensitive 3M Scotch® tape

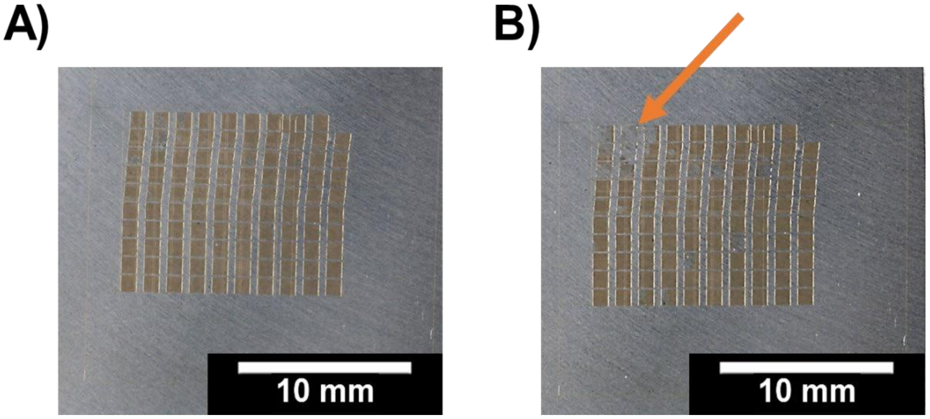

Figure 26. A) Sample A pre- tape pull-off adhesion testing and B) Sample A post- tape pull-off adhesion testing using the blue pressure sensitive 3M Scotch® tape

5.2 Pull-Off Adhesion Testing

To mitigate the limitations of the tape test, a standardized pull-off adhesion test, outlined in ISO 4624, was used to achieve quantitative measurements of AM printed inks on various substrate surfaces. In this work, a Defelsko Positest AT-A device was used for the pull-off testing. The Positest AT-A device features a self-aligning dolly system and is actuated by a hydraulic pump at a smooth and continuous rate. The tests were performed by bonding a dolly directly to the surface coating/film with an adhesive epoxy or glue and then subjected to a controlled tensile test (pull-off test) until the coating/substrate bond was broken (Figure 27). The pressure required to break the bond was measured, which enabled the quantification of adhesion. Figure 28 shows the progressive steps used in performing a pull-off adhesion test.

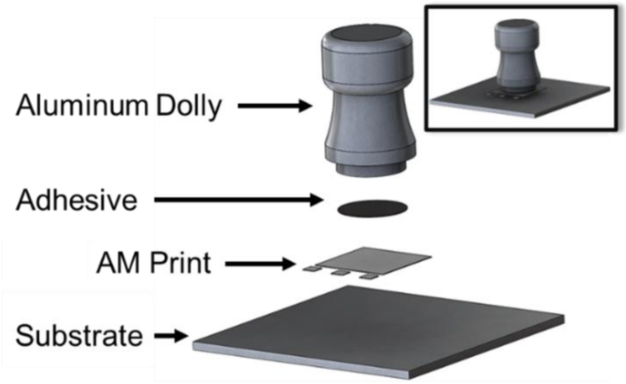

Figure 27. Schematic of the destructive pull-off tester for adhesion testing

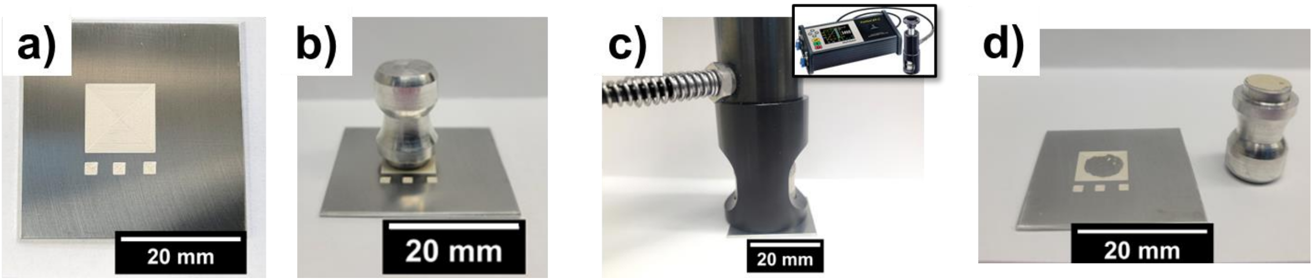

Figure 28. Flow diagram of the pull-off testing. a) the as-printed adhesion pad, b) dolly adhered to the printed pad, c) the hydraulic Delfesko Positest device mounted to the dolly, and d) sample after ink was removed from the pull-off test.

The ideal adhesion test result occurs when the interface between the print and the substrate fails. However, achieving 100% failure at this interface when performing the pull-off test may not always occur and often leads to a mix of failure modes (i.e., interface between glue and print, interface between glue and dolly, interface between print and substrate). As seen in Figure 29, the failure can occur between two interfaces (i.e., adhesive fracture) or within a layer (i.e., cohesive failure). These different failure modes will report a different break-off force during testing (Figure 30). As seen in Figure 30, the break off force of an ideal A/B adhesive failure (i.e., substrate/print failure) was found to be at about 1.86 MPa. Other failure modes either drastically increase or decrease the break-off force read by the pull-off test device and invalidate the adhesion strength of the print. To maximize the failure between the print and the substrate, an adhesive that provides a stronger bond than the print/glue and glue/dolly interface needs to be used. The adhesive must also not react to or affect the bond strength of the print.

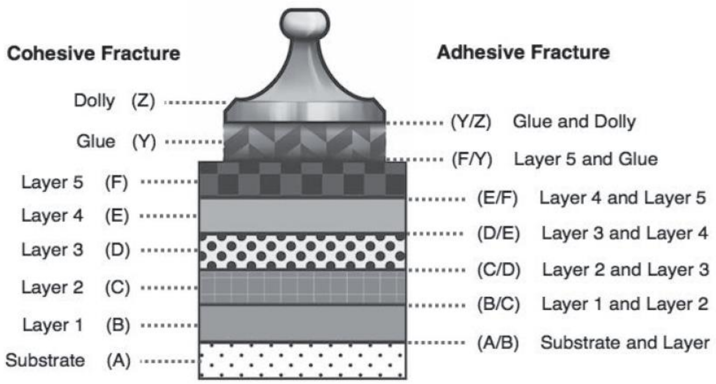

Figure 29. The different interfaces for failure for a multi-layer adhesion test [54].

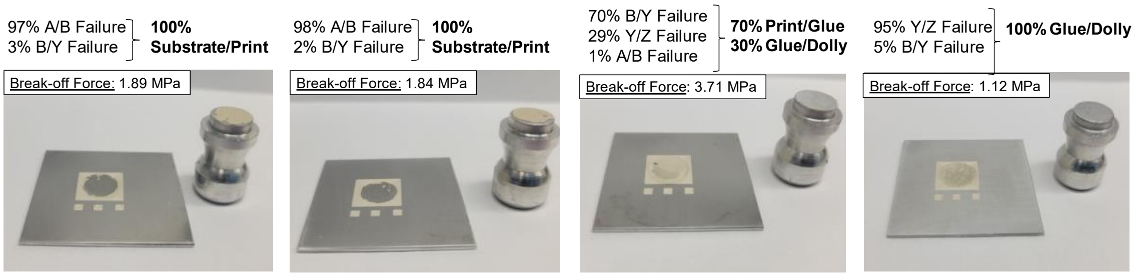

Figure 30. Break-off force of four different samples with varying failure modes. ISO 4624 states to round up the estimated failure mode to the nearest 10%.

As seen on Figure 31, the thicknesses of the prints can vary between 35 µm and 96 µm despite printing them on the same substrate with the same parameter. Figure 31c lists the samples from thinnest to thickest print and not in the order they were printed. The variation in thickness of the prints has implications for impacting the adhesion of the prints to the substrate and its potential application for certain laser-based adhesion measurement techniques.

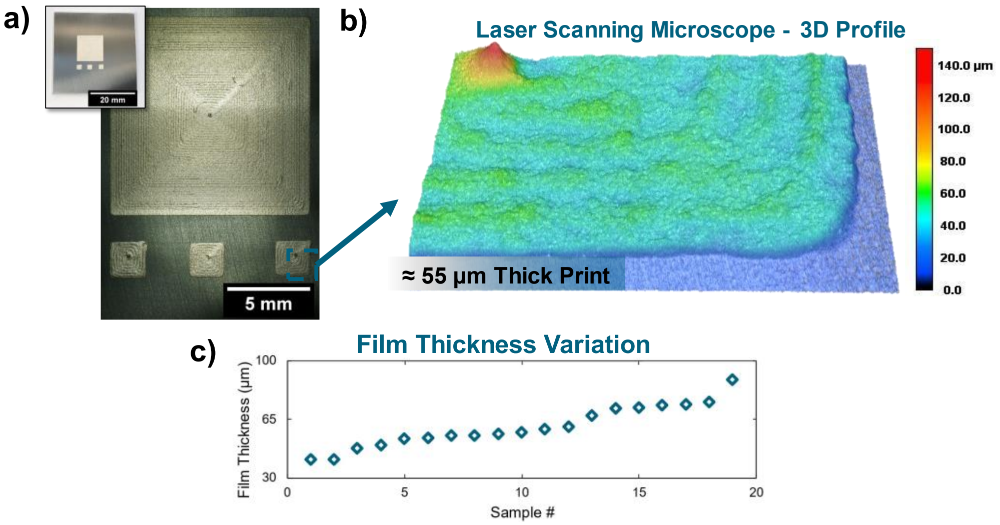

Figure 31. a) Representative photo of a pad printed for adhesion testing with a laser-based method and the pull-off tester. b) Thickness measured using a laser profilometer. c) A wide variation in thickness of 19

different pads printed with the same parameters; samples are listed from thinnest to thickest print (not in the order they were printed).

5.3 Laser-Induced Spallation

The laser-induced spallation technique was used as a complimentary approach to the pull-off testing to characterize the adhesion of the BST films printed using AJP on SS316 substrates. The laser spall method is an all-optical, non-contact, and locally-destructive experimental setup that has been used to measure the adhesion and interfacial properties of films/ coatings [55]. The Laser Shock System (LSS) at INL [56-58] was used for the laser-induced spallation experiments in this study and was previously to assess the adhesion of AJP printed silver films on aluminum 6061 substrates [59]. The interfacial adhesion strength between the film and substrate was determined from the velocity of a laser-generated shock/ stress wave that led to the onset of fracture/ spallation of the film/coating. In the LSS setup, stress waves were generated in the SS316L substrate using a Continuum Powerlite DLS pulsed laser (Model: PL+ 2J DLS) that emits 1064 nm laser pulses with a pulse duration of ~40 ns. A piece of layered tape (3M Scotchcal^{TM} High Performance Automotive Tape), comprising of a transparent polyvinyl chloride (PVC) film over a black-colored liner was applied to the free surface of the SS316L substrates opposite to that bearing the printed BST films. The black tape served as a medium for absorbing the optical energy of the incident laser pulses that subsequently led to generation of the shock/stress wave in the substrate via rapid thermoelastic expansion or ionization of the absorbing layer [55]. The transparent PVC film acted as the laser energy-confining layer that aids in the generation of high amplitude stress waves. The pulsed laser beam used to generate the stress wave was focused to a diameter of 3 mm on the absorbing tape layer. The surface velocity of the printed BST film induced by the stress/shock wave that was transmitted through the film/substrate interface was monitored using an interferometer derived from a Tecnar® pulsed detection laser system that was focused directly on the surface of the BST printed film. Figure 32a shows a schematic representation of the experimental geometry associated with the stress/ shock wave generation in the laser-induced spallation technique. Schematics of the film/substrate interface loading mechanism and interferometric detection of the shock wave velocity are shown in Figure 32b.
A key objective of the laser-induced spallation experiments was to determine whether subjecting the printed sensor to thermal cycling between room temperature and the target temperature of 500°C multiple times, or dwelling at 500°C for extended duration, would affect the adhesion between the printed BST insulation layer and the stainless-steel substrate. To this end, BST films printed on stainless steel 316L substrates were subject to: i) 5 heating/cooling cycles between room temperature and 500°C with a heating/ cooling rate of 5°C/minute; ii) 10 heating/cooling cycles between 200°C and 500°C at a heating rate of 5°C/minute, and passively air-cooled at a rate of approximately 5°C/minute; and iii) dwelling the samples at 500°C for 5 hours. Figure 33 shows SEM images at different magnification of the BST printed films in as-printed state, and after subjecting them to the three different thermal treatment scenarios. In all cases, the BST printed films exhibit considerable porosity, with micron-sized aggregates and some cracks clearly seen at longer length scales. It is evident from the SEM micrographs, however, that thermal cycling or dwelling for extended durations did not lead to cracking, flaking, or debonding of the BST film printed on the SS316L substrate. To the best of the authors' knowledge, there is no data reported on the coefficient of thermal expansion of BST films printed and sintered using direct-write techniques such as AJP. Nevertheless, the SEM observations provide strong evidence that the CTE mismatch between AJP printed BST and SS316L is not large enough to induce visible failure of the film/substrate bond.

BST films were printed in dimensions of 1 cm × 1 cm squares using AJP on stainless steel 316L substrates for the laser spall tests. The average thickness of the BST films, measured using laser profilometry, ranged from ~5 µm to ~22 µm. Prior to the laser spall tests, a BST film sample was exposed to the continuous wave (CW) laser beam from the interferometer used to measure the surface velocity for 30 seconds to determine if the CW detection laser beam did any damage to the printed film. Very minor damage, confined to lateral dimensions of ~10 µm × 10 µm, was seen on the BST film due to exposure to the CW interferometer beam. The damage is likely due to localized laser-induced heating. An optical image of the small-scale damage from the interferometer beam is shown in Figure 34.

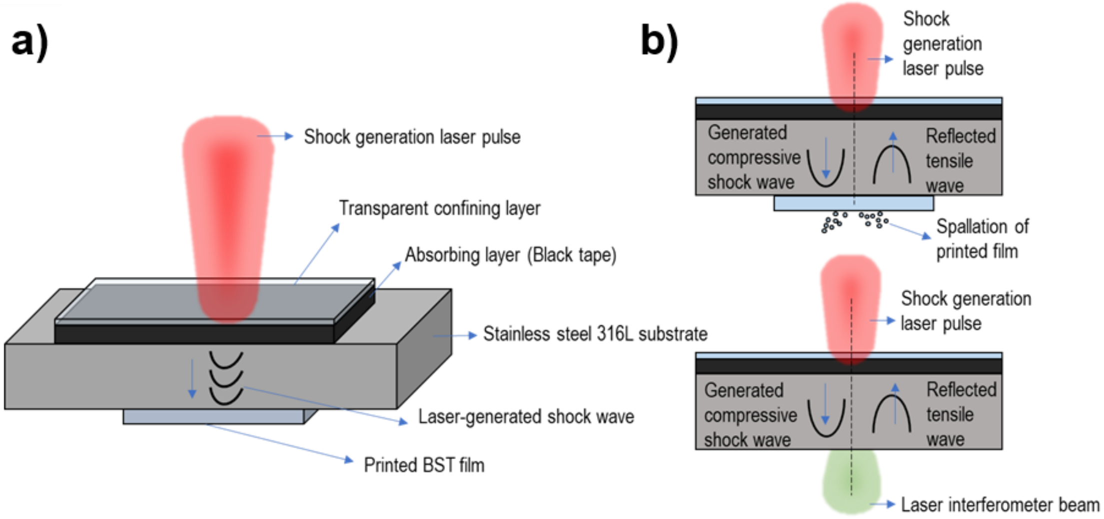

Figure 32. a) Schematic representation of the experimental geometry of the laser-induced spallation technique. b) Illustration of the spallation/fracture of the printed film by the laser-generated shock.

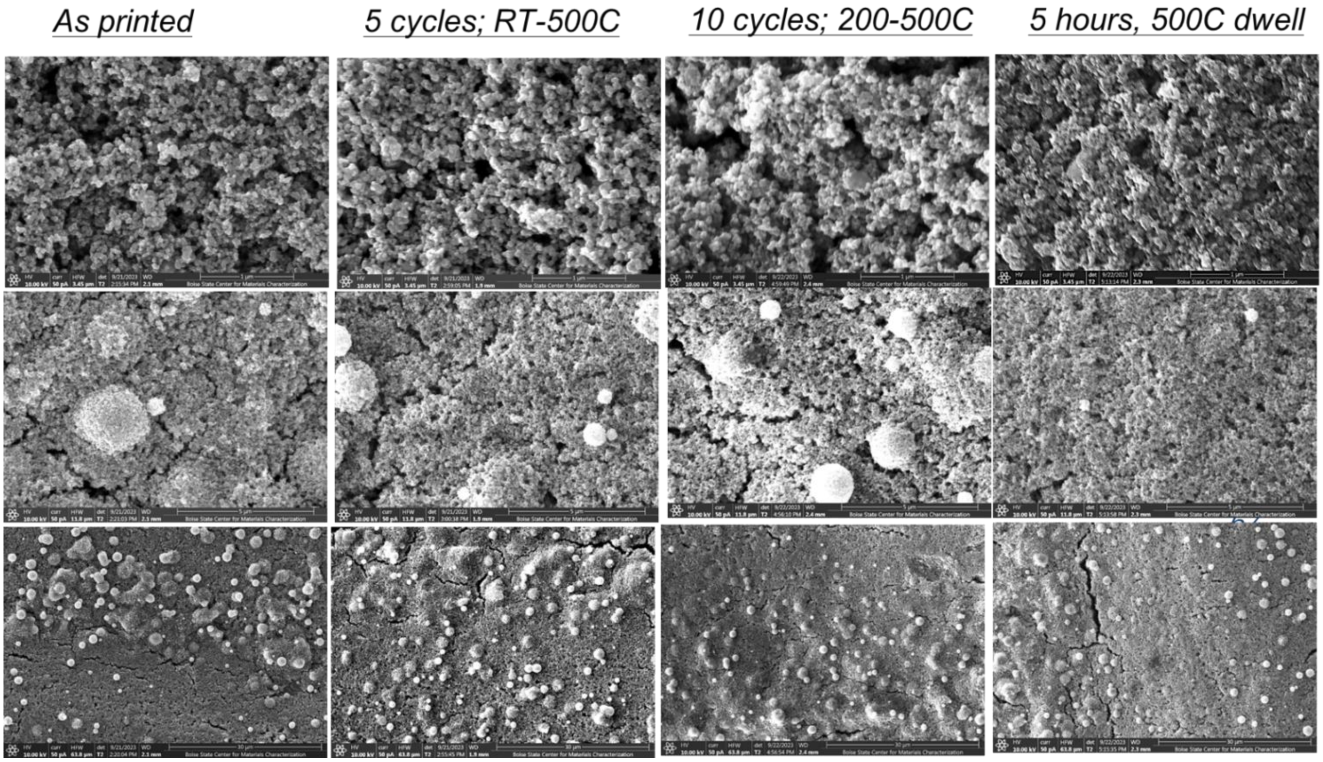

Figure 33. SEM images at different levels of magnification showing the morphology of the AJP printed BST films in i) as-printed condition; and after subjecting to ii) 5 cycles between room temperature and 500°C; iii) 10 cycles between 200°C and 500°C; and iv) a dwell at 500°C for 5 hours.

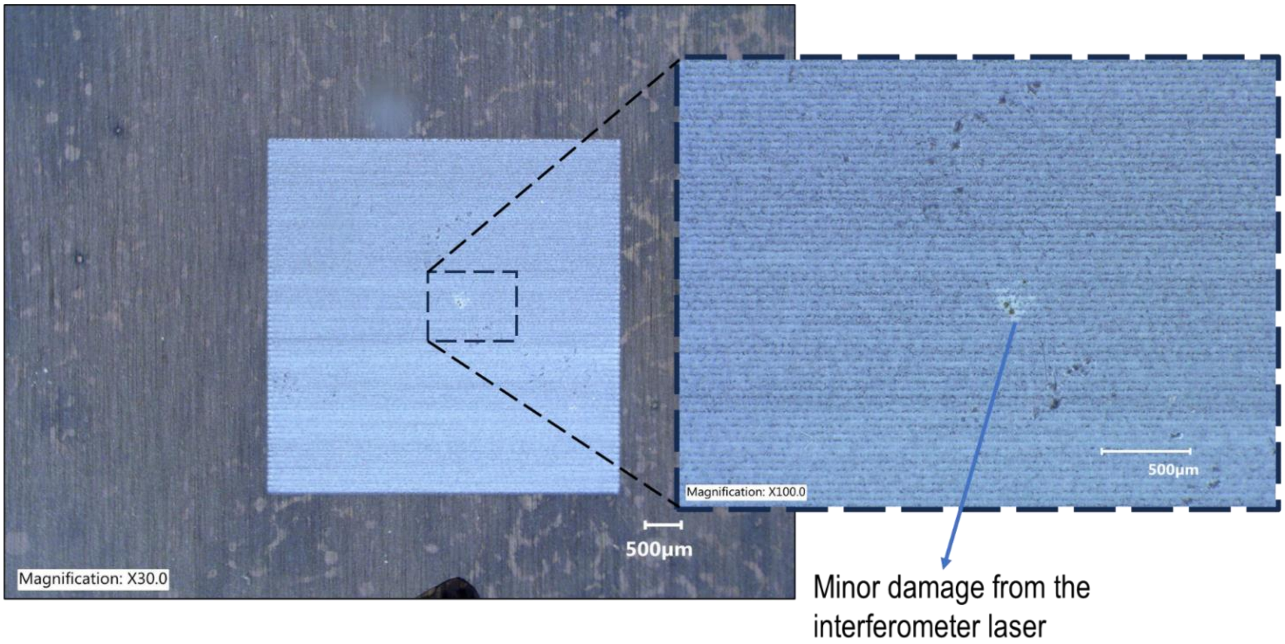

Figure 34. Optical microscope images highlighting the localized damage on the printed BST film caused by the interferometer laser beam at center of the detection area.

Laser spall tests were performed by generating shock waves in the SS316L substrate starting at the lowest laser pulse energy of 0.14 – 0.15 J that yielded a reliable interferometric signal of surface velocity. The measured surface velocity of BST film ranged between 16 – 30 m/s. This variation in the measured surface velocity at the same laser pulse energy is attributed to the differences in thickness of the BST film. Even at the lowest laser pulse energy of 0.14 – 0.15 J, spallation/ ejection of material from the laser-generated shock wave was observed. There were differences in the modes of failure between the different samples, however. Figure 35 shows optical images of an as-printed BST film subject to a laser shock generated from a laser pulse with an energy of 0.152 J. The surface velocity measured on the print was 30.1 m/s. The average thickness of this 1 cm × 1 cm printed pad was 8.1 µm. It is clear from Figure 35 that considerable BST material was ejected from the sample by the laser-generated shock wave. A closer inspection of the failure mode shows that BST material along the center line of each pass of the print remained adhered, and that material only from the periphery of each print pass was ejected by the laser-generated shock wave. To further investigate the morphology of each print pass, SEM imaging was performed on an as-printed BST film. Figure 36 shows the SEM micrograph of five print passes, spaced ~60 µm apart. The center of each print pass appears well consolidated and is noticeably thicker than the printed region on the periphery of each pass. Considerable overspray is noticed in the peripheral regions of each pass. The peripheral regions of each pass also contain some cracking and regions of unconsolidated BST material that appear as aggregates. The detachment of these peripheral regions along each print pass in the laser spall tests show that these regions are weakly bonded compared to the central region of each print pass. Previous studies have shown that the overspray region can be reduced by controlling the droplet size in aerosol jet printing [60]. The observation of ejection of the overspray regions of the print therefore provides pathways to refine AJP parameters for more resilient prints.

Figure 37 shows optical images in bright and dark field modes of another 1 cm × 1 cm as-printed BST film on SS316L subject to a laser-generated shock wave. The average thickness of this printed BST film was measured to be 5.21 µm, about 36% lower than the thickness of the print shown in Figure 35. The energy of the laser pulse that generated the shock wave was measured to be 0.146 J. This resulted in a measured surface velocity of 40.45 m/s on the BST film. This is considerably higher than the velocity of

30.1 m/s measured on the thicker print shown in Figure 35. The surface velocity measured on the thinner print was higher than that measured on the thicker print due to the lower shock wave attenuation in the thinner print. The morphology of the spalled region shown in Figure 37 shows a predominant cohesive failure, i.e., failure within the BST film itself, as opposed to failure at the film/substrate interface. This is evident from the fact that the bare stainless steel substrate is not visible from the microscope images in Figure 37. This also suggests that the overspray regions may be smaller in thinner prints. Our observations further underscore the need for accurate control of the dimensions (both lateral and out-of-plane) of each print pass during the AJP process.

Next, laser spall tests were performed on the BST prints subject to thermal cycling and extended duration dwells at 500°C. Figure 38 shows the spalled region of a printed BST sample subject to a static hold thermal dwell of 500°C for 5 hours. The average thickness of the 1 cm × 1 cm shown in Figure 38 was measured to be 10.27 µm. The incident laser pulse, with an energy of 0.146 J, resulted in a peak surface velocity of 28.84 m/s on the BST film. The morphology of the spalled region is very similar to that of the as-printed film shown in Figure 35. This includes the failure predominantly in the peripheral region of each print pass (in the overspray region), with BST printed material in the center of each pass still adhered to the substrate. The peak surface velocity measured on the BST film subject to the 5 hour dwell at 500°C was also very close to that measured on an as-printed BST film of equivalent thickness. This indicates that the attenuation of the shock wave (and therefore mechanical stiffness) of the printed BST film did not show considerable change after the 5 hour heat treatment. Similar observations were made on the BST films subject to thermal cycling. Therefore, while the laser spall tests show that the adhesion of the overspray regions of thicker prints (with a thickness greater than ~8 µm) is lower than that of the printed material along the central region of each pass, the BST material itself remains resilient and shows little change in failure morphology and elastic properties (inferred from the attenuation of the shock wave through the BST film).

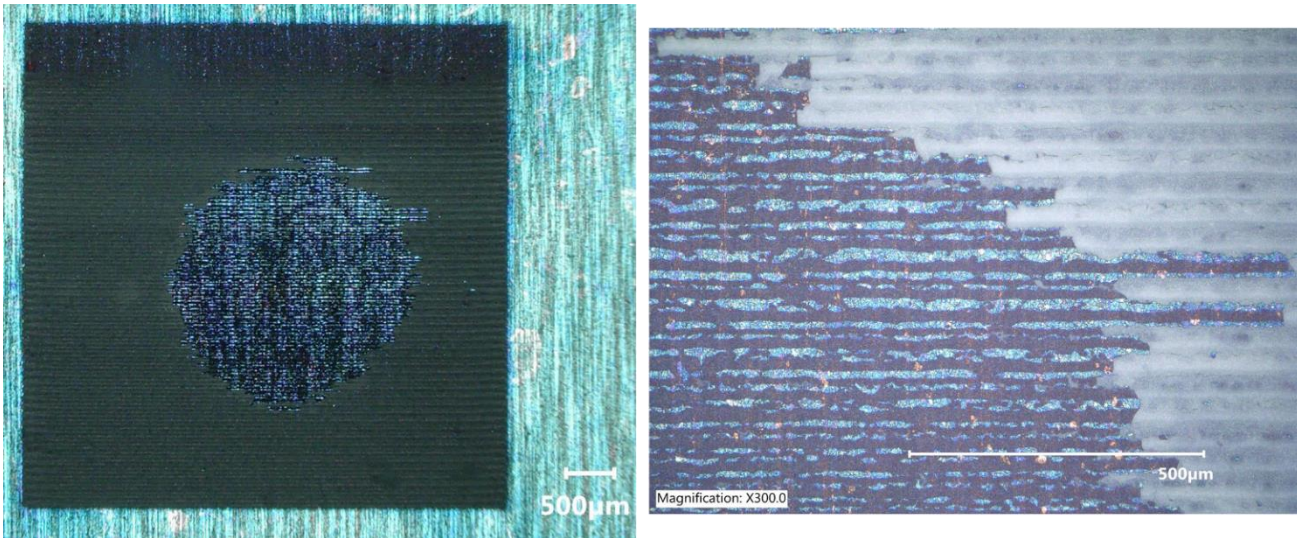

Figure 35. Optical images of a BST printed film subject to a laser-generated shock wave from a laser pulse with an energy of 0.152 J. The zoomed-in view of the damaged region shows material ejection from the periphery of each print, while material from the center line of each print pass remained adhered to the substrate.

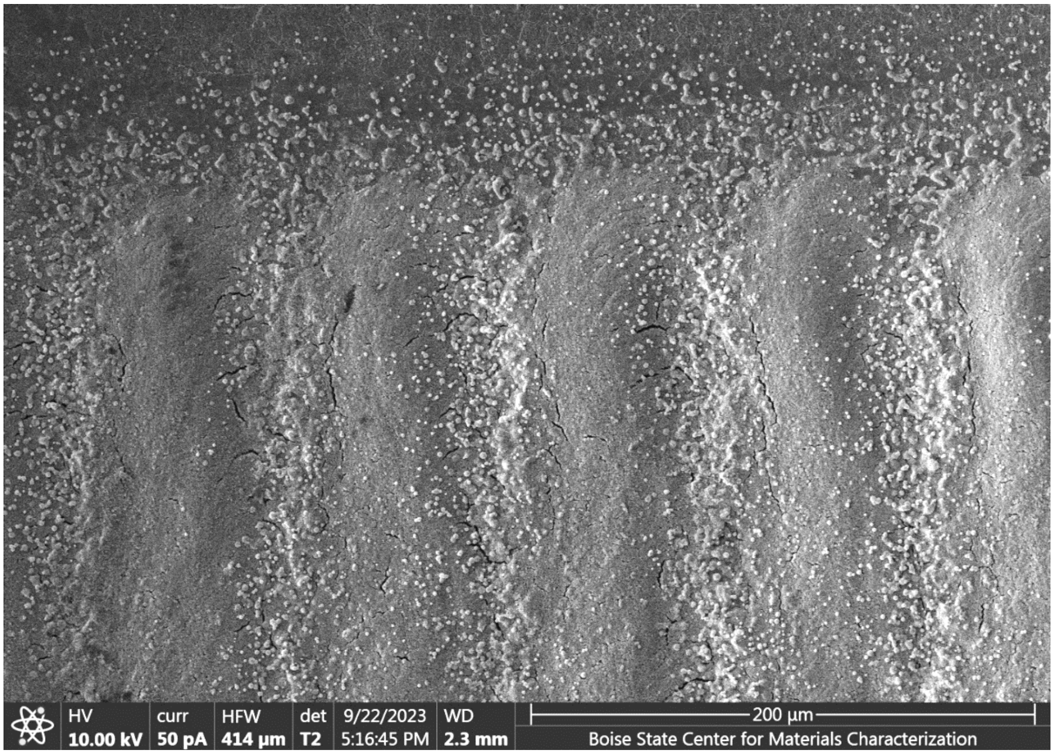

Figure 36. SEM image of five print passes of an as-printed BST film.

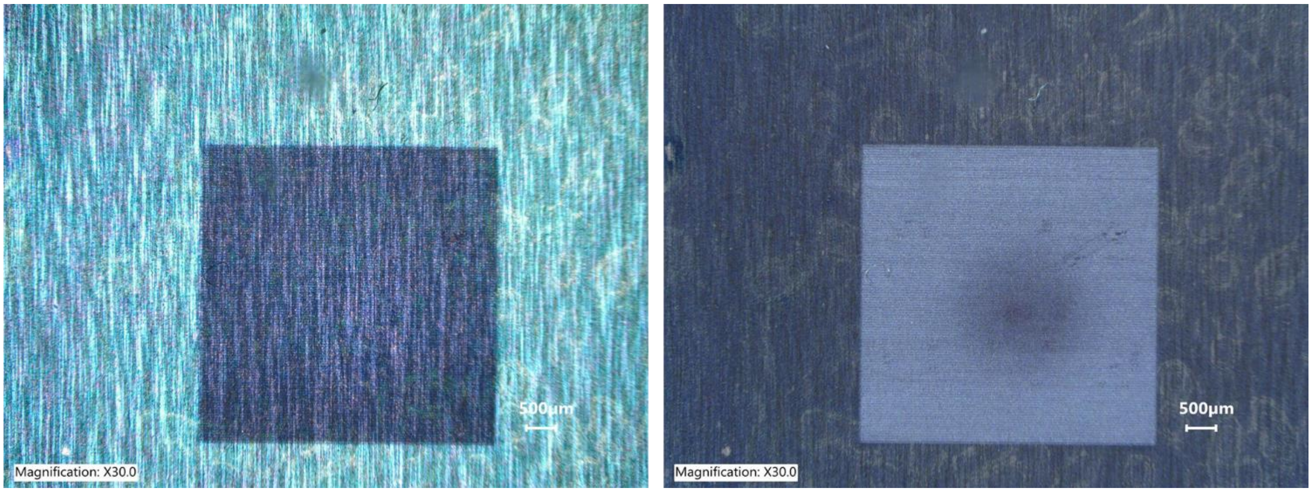

Figure 37. Optical microscope images in bright (left) and dark (right) field modes of a BST print subject to a laser-generated shock wave from a 0.146 J laser pulse.

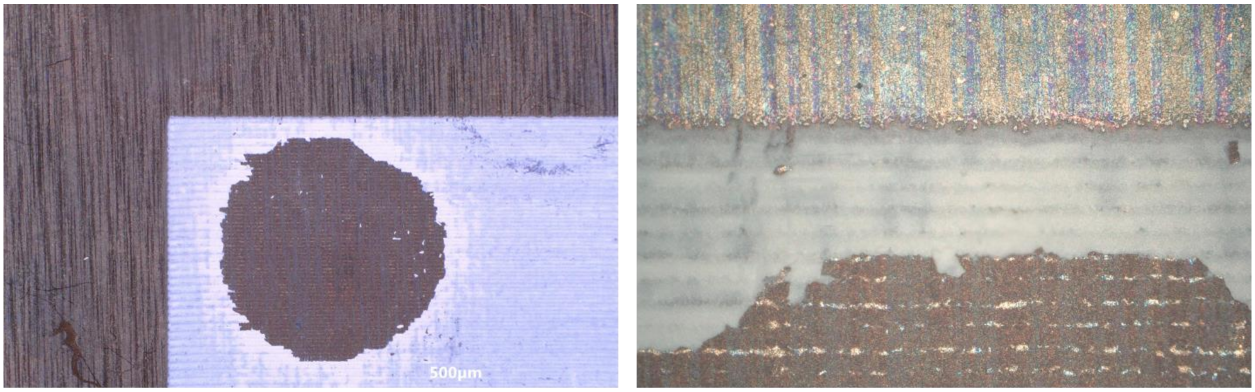

Figure 38. Spalled region of a BST printed film subject to a static hold at 500°C for 5 hours. The morphology of the failed region is very similar to that of the thicker as-printed BST film shown in Figure 35.

6. SUMMARY AND CONCLUSION

The IDE CSGs were initially fabricated on Al6061 and SS316 substrates with polyimide insulation. The CSG was mechanical strain up to 0.11% strain at temperatures up to 300°C. The CSGs with polyimide insulation showed high reproducibility when compared to the commercial bondable, free-filament RSGs. In addition, the IDE CSGs also exhibited predictable strain sensing performance as they matched well with previously developed analytical models. Having a CSG that is reproducible and predicable in performance are two factors that are important when deploying the strain gauges in field-conditions and costly, time-consuming experiments (e.g., test reactor facilities).

To increase the operating temperature of the IDE CSG above 300°C, BST was investigated as a feasible insulation/encapsulation material as it has been shown to have a changing dielectric permittivity (i.e., dielectric constant) with strain. To enable its application for the printed IDE CSGs, BST ink was successfully formulated to print with an aerosol jet printer on both flat and conformal surfaces. The ink formulation was tailored to reduce the film thickness, which helped minimize large observable defects and cracks on the surface of the printed film. The printing process parameters was also improved to enable the deposition of large area prints (i.e., > 100 mm^2) with uniform film thickness. The dielectric properties of the BST film were measured during a thermal transient and dwell up to 500°C. The effective dielectric constant of BST on SS316 was found to be stable during a five-hour thermal dwell at 500°C. A stable dielectric constant is important as drifting of the dielectric constant in isothermal conditions is a source of measurement error for the IDE CSG. The initial performance of the IDE CSG on printed BST were tested at room temperature and 500°C. In addition to measurement error from external parasitic capacitance, the porosity and micron-scale cracks observed throughout the current fabricated BST film was found to impact the sensitivity and functionality of the IDE CSG at room temperature and 500°C, respectively.

A combination of quasi-static and dynamic test methods was used to evaluate the resilience and robustness of the BST film that will form the insulating layer in the printed IDE CSGs. While the tape test did not provide qualitative results, the pull-off tests showed that thickness variations in the printed BST films can lead to different failure morphologies. The laser spall tests also showed the BST films of different thickness led to different failure morphologies. Thinner BST prints (with a thickness of less than 8 µm) showed an almost complete cohesive failure, indicating that the film/substrate adhesion was stronger than the adhesion between the fused BST nanoparticles themselves. In the thicker prints (with a thickness greater than 8 µm), failure occurred at the film/substrate only in the overspray regions at the periphery of each print pass, while the BST material at the center of each print pass remained adhered. Our findings suggest that an AJP process parameters that minimize the overspray region and keep the thickness to less than 8 µm can result in consistent and robust printed insulation layers for IDE CSGs.

7. REFERENCES

[1] N. Shahrubudin, T.C. Lee, R. Ramlan, An overview on 3D printing technology: Technological, materials, and applications, Procedia Manufacturing, 35(2019) 1286-96.
[2] T. Pandhi, E. Kreit, R. Aga, K. Fujimoto, M.T. Sharbati, S. Khademi, et al., Electrical Transport and Power Dissipation in Aerosol-Jet-Printed Graphene Interconnects, Sci Rep-Uk, 8(2018) 1-10.
[3] K.T. Fujimoto, L.A. Hone, K.D. Manning, R.D. Seifert, K.L. Davis, J.N. Milloway, et al., Additive Manufacturing of Miniaturized Peak Temperature Monitors for In-Pile Applications, Sensors, 21(2021) 7688.
[4] M.T. Rahman, R. Moser, H.M. Zbib, C.V. Ramana, R. Panat, 3D printed high performance strain sensors for high temperature applications, J Appl Phys, 123(2018) 1-12.
[5] S. Vella, C. Smithson, K. Halfyard, E. Shen, M. Chretien, Integrated capacitive sensor devices aerosol jet printed on 3D objects, Flex Print Electron, 4(2019) 1-16.
[6] R. Salary, J.P. Lombardi, M.S. Tootooni, R. Donovan, P.K. Rao, P. Borgesen, et al., Computational Fluid Dynamics Modeling and Online Monitoring of Aerosol Jet Printing Process, J Manuf Sci E-T Asme, 139(2017) 1-21.
[7] H.N. Zhang, S.K. Moon, T.H. Ngo, 3D Printed Electronics of Non-contact Ink Writing Techniques: Status and Promise, Int J Precis Eng Manuf-Green Technol, 7(2020) 511-24.
[8] J.J. Adams, E.B. Duoss, T.F. Malkowski, M.J. Motala, B.Y. Ahn, R.G. Nuzzo, et al., Conformal Printing of Electrically Small Antennas on Three-Dimensional Surfaces, Adv Mater, 23(2011) 1335-40.
[9] M. Smith, Y.S. Choi, C. Boughey, S. Kar-Narayan, Controlling and assessing the quality of aerosol jet printed features for large area and flexible electronics, Flex Print Electron, 2(2017) 1-11.
[10] K.T. Fujimoto, J.K. Watkins, T. Phero, D. Litteken, K. Tsai, T. Bingham, et al., Aerosol jet printed capacitive strain gauge for soft structural materials, npj Flexible Electronics, 4(2020) 1-9.
[11] S.R. Kim, J.H. Kim, J.W. Park, Wearable and Transparent Capacitive Strain Sensor with High Sensitivity Based on Patterned Ag Nanowire Networks, Acs Appl Mater Inter, 9(2017) 26407-16.
[12] H. Nesser, J. Grisolia, T. Alnasser, B. Viallet, L. Ressier, Towards wireless highly sensitive capacitive strain sensors based on gold colloidal nanoparticles, Nanoscale, 10(2018) 10479-87.
[13] ASTM, E1319 - 98: Standard Guide for High-Temperature Static Strain, ASTM, (2014) 971-81.
[14] B. Noltingk, D. McLachlan, C. Owen, P. O'neill, High-stability capacitance strain gauge for use at extreme temperatures, Proceedings of the Institution of Electrical Engineers, IET1972, pp. 897-903.
[15] K.L. Ranganatha, K. Novich, T. Phero, K.T. Fujimoto, D. Litteken, D. Estrada, et al., A Wireless, Multi-Channel Printed Capacitive Strain Gauge System for Structural Health Monitoring, 2021 IEEE Sensors, IEEE, pp. 1-4.
[16] C.F. Hu, J.Y. Wang, Y.C. Liu, M.H. Tsai, W.L. Fang, Development of 3D carbon nanotube interdigitated finger electrodes on polymer substrate for flexible capacitive sensor application, Nanotechnology, 24(2013) 1-14.
[17] R. Matsuzaki, A. Todoroki, Wireless flexible capacitive sensor based on ultra-flexible epoxy resin for strain measurement of automobile tires, Sensor Actuat a-Phys, 140(2007) 32-42.
[18] E.R. Cholleti, J. Stringer, P. Kelly, C. Bowen, K. Aw, Mechanical Behaviour of Large Strain Capacitive Sensor with Barium Titanate Ecoflex Composite Used to Detect Human Motion, Robotics, 10(2021) 1-21.

[19] Č. Žlebič, N. Ivanišević, M. Kisić, N. Blaž, A. Menićanin, L. Živanov, et al., Comparison of resistive and capacitive strain gauge sensors printed on polyimide substrate using ink-jet printing technology, 2014 29th International Conference on Microelectronics Proceedings-MIEL, IEEE, pp. 141-4.
[20] J. Li, J.P. Longtin, S. Tankiewicz, A. Gouldstone, S. Sampath, Interdigital capacitive strain gauges fabricated by direct-write thermal spray and ultrafast laser micromachining, Sensors and Actuators A: Physical, 133(2007) 1-8.
[21] S. Ren, S. Jiang, H. Liu, W. Zhang, Y. Li, Investigation of strain gauges based on interdigitated Ba0. 5Sr0. 5TiO3 thin film capacitors, Sensors and Actuators A: Physical, 236(2015) 159-63.
[22] M. Gerber, C. Weaver, L.E. Aygun, N. Verma, J.C. Sturm, B. Glišić, Strain transfer for optimal performance of sensing sheet, Sensors-Basel, 18(2018) 1907.
[23] R. Zeiser, T. Fellner, J. Wilde, Capacitive strain gauges on flexible polymer substrates for wireless, intelligent systems, Journal of Sensors and Sensor Systems, 3(2014) 77-86.
[24] T.L. Phero, K.A. Novich, B.C. Johnson, M.D. McMurtrey, D. Estrada, B.J. Jaques, Additively manufactured strain sensors for in-pile applications, Sensors and Actuators A: Physical, (2022) 113691.
[25] T.R. Filanc-Bowen, G.H. Kim, Y.M. Shkel, Novel sensor technology for shear and normal strain detection with generalized electrostriction, 2002 IEEE Sensors, IEEE, pp. 1648-53.
[26] J.-Q. Huang, Q.-A. Huang, M. Qin, W. Dong, X. Chen, Strain effect of the dielectric constant in silicon dioxide, Journal of microelectromechanical systems, 19(2010) 1521-3.
[27] ASTM, E8/E8M - 16a: Standard Test methods for Tension Testing of Metallic Materials, ASTM.
[28] L. Shu, X.M. Wang, L. Li, D.W. Yan, L.P. Peng, L. Fan, et al., The investigation of integrated SAW strain sensor based on AlN/TC4 structure, Sensor Actuat a-Phys, 293(2019) 14-20.
[29] A. Hammoud, E. Baumann, E. Overton, I. Myers, J. Suthar, W. Khachen, et al., High temperature dielectric properties of Apical, Kapton, PEEK, Teflon AF, and Upilex polymers, [Proceedings] 1992 Annual Report: Conference on Electrical Insulation and Dielectric Phenomena, IEEE, pp. 549-54.
[30] J.D. Tucker, Y.R. Wei, W.R. Marcum, P.V. Murkute, B.J. Gibbons, O.B. Isgor, Quantifying Oxide Layer Growth at Low Pressures and Temperatures for Aluminum Alloy 6061, Metall Mater Trans A, 50a(2019) 3388-98.
[31] ASTM, E251 - 92: Standard Test Methods for Performance Characterisitics of Metallic Bonded Resitance Strain Gauges, ASTM, (2014) 433-52.
[32] Migrating from a Keysight 4284A LCR Meter to a Keysight E4980A Precision LCR Meter - Technical Overview, Keysight Technology, 2014, pp. 1-28.
[33] J.G. Kaufman, Properties of aluminum alloys: tensile, creep, and fatigue data at high and low temperatures: ASM international; 1999.
[34] J. Kaufman, Properties and characteristics of aluminum and aluminum alloys, ASM International: Geauga, OH, USA, (2016) 1-9.
[35] R. Herbert, S. Mishra, H.R. Lim, H. Yoo, W.H. Yeo, Fully Printed, Wireless, Stretchable Implantable Biosystem toward Batteryless, Real-Time Monitoring of Cerebral Aneurysm Hemodynamics, Adv Sci, (2019) 12.
[36] Q.S. Jing, Y.S. Choi, M. Smith, C.L. Ou, T. Busolo, S. Kar-Narayan, Freestanding Functional Structures by Aerosol-Jet Printing for Stretchable Electronics and Sensing Applications, Adv Mater Technol, 4(2019) 1-9.
[37] M. Serpelloni, E. Cantu, M. Borghetti, E. Sardini, Printed Smart Devices on Cellulose-Based Materials by means of Aerosol-Jet Printing and Photonic Curing, Sensors-Basel, 20(2020) 18.
[38] T. Shaw, Z. Suo, M. Huang, E. Liniger, R. Laibowitz, J. Baniecki, The effect of stress on the dielectric properties of barium strontium titanate thin films, Appl Phys Lett, 75(1999) 2129-31.
[39] C.S. Hwang, S.O. Park, H.J. Cho, C.S. Kang, H.K. Kang, S.I. Lee, et al., Deposition of extremely thin (Ba, Sr) TiO3 thin films for ultra-large-scale integrated dynamic random access memory application, Appl Phys Lett, 67(1995) 2819-21.
[40] C. Chen, H. Feng, Z. Zhang, A. Brazdeikis, Z. Huang, W. Chu, et al., Epitaxial ferroelectric Ba 0.5 Sr 0.5 TiO 3 thin films for room-temperature tunable element applications, Appl Phys Lett, 75(1999) 412-4.

[41] P. Joshi, M. Cole, Mg-doped Ba 0.6 Sr 0.4 TiO 3 thin films for tunable microwave applications, Appl Phys Lett, 77(2000) 289-91.
[42] A. Chaabani, A. Njeh, W. Donner, A. Klein, M.H.B. Ghozlen, Elasticity study of textured barium strontium titanate thin films by X-ray diffraction and laser acoustic waves, Japanese Journal of Applied Physics, 56(2017) 055501.
[43] H. Abomostafa, M. Ellamey, Studying the mechanical properties of barium strontium titanate ceramics by an ultrasonic pluse echo technique, J Ovonic Res, 14(2018) 307-16.
[44] M. Schneider, J. Maurath, S.B. Fischer, M. Weiß, N. Willenbacher, E. Koos, Suppressing crack formation in particulate systems by utilizing capillary forces, Acs Appl Mater Inter, 9(2017) 11095-105.
[45] B.S. Tomar, A. Shahin, M.S. Tirumkudulu, Cracking in drying films of polymer solutions, Soft Matter, 16(2020) 3476-84.
[46] O.K. Ranasingha, M. Haghzadeh, M.J. Sobkowicz, E. Kingsley, C. Armiento, A. Akyurtlu, Formulation and Characterization of Sinterless Barium Strontium Titanate (BST) Dielectric Nanoparticle Ink for Printed RF and Microwave Applications, J Electron Mater, 50(2021) 3241-8.
[47] H.A. Gatea, I.S. Naji, The effect of Ba/Sr ratio on the Curie temperature for ferroelectric barium strontium titanate ceramics, Journal of Advanced Dielectrics, 10(2020) 2050021.
[48] L. Cai, L. Song, P.S. Luan, Q. Zhang, N. Zhang, Q.Q. Gao, et al., Super-stretchable, Transparent Carbon Nanotube-Based Capacitive Strain Sensors for Human Motion Detection, Sci Rep-Uk, 3(2013) 1-9.
[49] M.R. Werner, W.R. Fahrner, Review on materials, microsensors, systems and devices for high-temperature and harsh-environment applications, IEEE Trans Ind Electron, 48(2001) 249-57.
[50] E. Brachmann, M. Seifert, D. Ernst, S.B. Menzel, T. Gemming, Pt-wire bonding optimization for electroplated Pt films on gamma-Al2O3 for high temperature and harsh environment applications, Sensor Actuat a-Phys, 284(2018) 129-34.
[51] J. Yin, Z.X. Liang, J.D. van Wyk, High temperature embedded SiC chip module (ECM) for power electronics applications, IEEE Trans Power Electron, 22(2007) 392-8.
[52] A. Hassan, Y. Savaria, M. Sawan, Electronics and packaging intended for emerging harsh environment applications: A review, IEEE Transactions on Very Large Scale Integration (VLSI) Systems, 26(2018) 2085-98.
[53] M. Rezaee, L.-C. Tsai, M.I. Haider, A. Yazdi, E. Sanatizadeh, N.P. Salowitz, Quantitative peel test for thin films/layers based on a coupled parametric and statistical study, Sci Rep-Uk, 9(2019) 19805.
[54] E.C.f. Standardization, DIN EN ISO 4624: 2016-08 Paints and Varnishes—Pull-off Test for Adhesion (ISO 4624: 2016), European Committee for Standardization Brussels, Belgium2016.
[55] H. Ehsani, J.D. Boyd, J. Wang, M.E. Grady, Evolution of the laser-induced spallation technique in film adhesion measurement, Applied Mechanics Reviews, 73(2021) 030802.
[56] J. Smith, C. Scott, B. Benefiel, B. Rabin, Interface characterization within a nuclear fuel plate, Applied Sciences, 9(2019) 249.
[57] J.A. Smith, J.M. Lacy, C.L. Scott, B.C. Benefiel, D. Lévesque, J.-P. Monchalin, et al., Further investigation of surface velocity measurements for material characterization in laser shockwave experiments, AIP Conference Proceedings, AIP Publishing2018.
[58] J.A. Smith, J.M. Lacy, D. Lévesque, J.-P. Monchalin, M. Lord, Use of the Hugoniot elastic limit in laser shockwave experiments to relate velocity measurements, AIP Conference Proceedings, AIP Publishing2016.
[59] T.L. Phero, A.R. Khanolkar, K.T. Fujimoto, J.A. Smith, M.D. McMurtrey, Development of Quality Control Methods for Robust and Reliable Sensor Design, Idaho National Lab.(INL), Idaho Falls, ID (United States)2022.
[60] G. Chen, Y. Gu, H. Tsang, D.R. Hines, S. Das, The effect of droplet sizes on overspray in aerosol-jet printing, Adv Eng Mater, 20(2018) 1701084.